Free vibration of fully coupled thermoelastic multilayered composites with imperfect interfaces

Aurélien Vattré, Ernian Pan, Vincent Chiaruttini

Free vibration of fully coupled thermoelastic multilayered composites with imperfect interfaces

A. Vattré[a,*], E. Pan[b], V. Chiaruttini[a]

[a] *Université Paris-Saclay, ONERA, Matériaux et Structures, 92322, Châtillon, France*
[b] *Department of Civil Engineering, University of Akron, Akron, OH 44325, United States*

Abstract

A fully coupled thermoelastic framework is formulated to cope with the free vibration response of anisotropic multilayered plates in three dimensions. The laminated structure consists of homogeneous laminae of arbitrary thickness and width under simply supported edge conditions in thermal environment. The general and exact field expressions of the temperature, heat flux, displacement and stress components are expressed in terms of double Fourier series expansions in any rectangular plate, which lead to the extended Stroh formalism with thermomechanical coupling effects in a concise and compact matrix form. Different imperfect interface conditions are introduced to characterize specific structural and thermal contact properties at the bounding interfaces, and further to determine the finite complex valued coefficients in the suitable series relations. The complete time-harmonic solutions in the laminated composites in the presence of perfect/imperfect interfaces are recursively obtained by means of the modified dual variable and position technique with explicit layer-to-layer transfer matrices. Results are obtained for different layups, length-to-thickness ratios and interfacial boundary conditions for two application examples, namely the graphite/epoxy cross-ply composites and the thermal barrier coatings on superalloys, without suffering from numerical exponential instability. These investigations reveal that the natural frequencies and first and higher vibration mode shapes of the multilayered structures can be considerably affected by increasing the environmental temperature and the severity of the interfacial imperfections. Since the through-thickness stress distribution in 2, 5, and 10 layered composites appears to be strongly correlated to the layups, such modal stress analysis could be exploited to locate the fatigue hotspots operated in dynamic structures and to guide the structural design of aircraft and spacecraft composite laminates subjected to residual vibrations.

Keywords: Thermoelasticity, fully coupling effects, anisotropy, free vibration, multilayered plate, imperfect interface, recursive field solutions

1. Introduction

Multilayer composites are largely used in the aeronautical and aerospace industries as well as modern high-technology sectors from low-cost manufacturing of semiconductor and thin-film devices to high-value added functional products in medicine. In contrast with monolithic samples, such laminated structures are composed of several homogeneous plates with desirable functional properties and specific arrangements to provide improved combinaisons of strength and ductility with attractive strength-to-weight and stiffness-to-weight ratios. The constant demand to move towards the most efficient and performant structures in aircraft and spacecraft engines is pushing the operating temperatures of the structural components to unprecedented levels [1, 2]. In severe temperature conditions combined with high frequency vibration events in gas-turbine engines, the thermal stresses and thermo-mechanical coupling effects play a crucial role in the structural integrity and operational life of aircraft materials and structures, including thermal barrier coatings for Ni-based superalloys as well as ceramic-matrix composites. Due to open-mode delamination of these multilayered structures in the critical thermal environment, externally forced and free vibration responses in damage prediction are considered in the earlier stages of the structural design process. In this respect, the present work focuses on a fully coupled thermo-mechanical formulation for the vibration response of simply supported composite laminates using anisotropic thermoelasticity theory in three dimensions.

*Email address: aurelien.vattre@onera.fr

The theory of thermoelasticity represents a generalization of both the classical linear elasticity and heat conduction theories in isotropic and anisotropic solids. It is therefore considered as an extension of the standard theory of isothermal elasticity, within which the deformation and stress states are produced not only by mechanical forces, but also by thermal forces due to temperature changes. The effect of the temperature field on the deformation state is also not a one-way phenomenon [3–6] since a local deformation of the body leads to temperature variation such that both mechanical and thermal characteristics are undoubtedly coupled, removing the paradox inherent in the classical uncoupled theory of thermoelasticity. In most practical engineering problems, however, the effect of the strain rate in the heat conduction equation has been neglected in the static, quasi-static and dynamic problems of thermoelasticity, including the forced and free vibration analysis of isotropic, orthotropic, laminated composite, sandwich and functionally graded plates with temperature-dependent material properties in thermal environments. Along this line, various analytical investigations using exact closed-form thermoelastic solutions [7–13], classical and higher-order plate theories [14–18], hierarchical Ritz-based models [19, 20] and numerical finite-element approaches [21–26] have been widely proposed for thermal analysis of homogeneous and heterogeneously laminated plates. In the aforementioned approaches, the partially coupled governing equations for the displacement field solutions require a priori the temperature distribution along the thickness direction, thus separately determined through thermal analysis alone and then prescribed for subsequent stress analysis. On the other hand, when the time variation of thermal sources in homogeneous and specially heterogeneous materials for most advanced aircraft structures is comparable with other terms in the heat conduction equation, the inverse effect in which the strain rate contributes to the temperature change must be included. The corresponding field solutions in terms of displacements and temperature must therefore be obtained through the fully coupled equations of thermoelasticity. While relevant fully coupled thermo-mechanical models have been proposed in the open literature, these two-side coupling approaches have been applied to various semi-analytical and numerical problems with different balance among accuracy, efficiency and robustness, within which both temperature and displacement fields are primary variables in the governing and constitutive equations [27–38]. The present approach fits into the second category of fully coupled models applied to anisotropic multilayered materials in presence of structurally and thermally imperfect boundary conditions at internal interfaces. The effect of such interfacial imperfections on the free vibration response of fully coupled thermoelastic multilayered composites has not yet been treated.

Interfacial imperfections represent a significant factor in the failure of laminated composite materials, which are evidenced by large local gradients of the field solutions close to the intrinsic interfaces. Compared to single layer structures, delamination and interface debonding in multilayered materials are also of great importance in designing modern aerospace composite structures, causing stiffness and strength degradation as well as reduction in the thermal reduction of the contacting dissimilar materials. While the common assumption of ideal perfectly bonded conditions at interfaces between adjoining plates is conducted by most of the previous works, structural imperfections can be applied by using the spring-type model [39–41], for which the components of the displacement jump are assumed to be linearly proportional to the interfacial traction components. Furthermore, weakly conducting interfaces can be taken into account by imposing Kapitza contact thermal resistance with a temperature jump proportional to the normal heat flux at the internal boundary [42], whereas a discontinuity in the normal heat flux across the interface is used to describe highly conducting interfaces [43–45]. These imperfect mechanical and thermal contacts between constituents are incorporated in the extended Stroh formalism, which is consistently formulated by completing the traditional propagation matrix method with the dual variable and position technique to overcome numerical instability issues at high frequency and wavenumber [13, 46]. The principal motivation is therefore to investigate the dependance of the environmental temperature and the interfacial properties on the eigenfrequencies and the corresponding first and higher eigenmode shapes of free vibration systems composed of anisotropic heterogeneous multilayered structures with possible large difference in material stiffnesses.

The Stroh formalism [47–49] provides exact solutions to the governing equations of anisotropic elasticity under generalized plane-strain deformations in terms of analytic functions. Using Fourier series representation, field solutions have been derived to describe

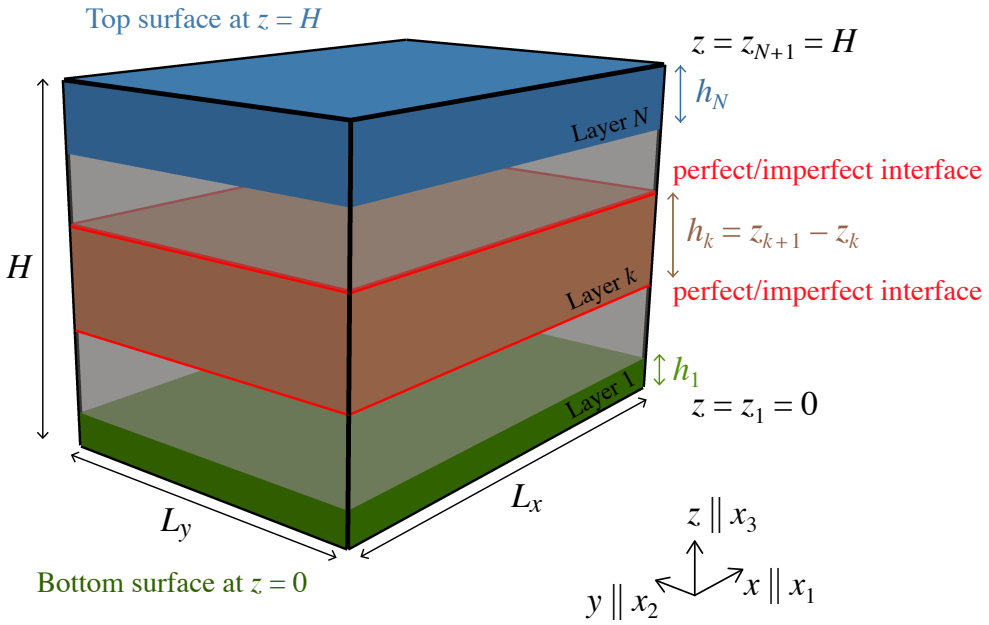

Figure 1: Three-dimensional schematics of a multilayered anisotropic system for free vibration analysis. In presence of perfect/imperfect internal interfaces, the laminated structure is arbitrarily composed of N homogeneous, orthotropic and rectangular layers with specific thermoelastic properties.

the thermoelastic deformations of anisotropic laminated plates subjected to arbitrary mechanical and thermal interface conditions at the edges [8, 12, 13], in which the external and internal boundary conditions are commonly used to determine the coefficients in the series expansions. The present formulation is also extended to the fully coupled thermoelastic problems of free vibration of multilayered structures with interfacial imperfections. The paper falls into four parts and is organized as follows. The fully coupled boundary-value problem is described in Section 2. In Section 3, the general time-harmonic solutions for each homogeneous plates are derived by means of double Fourier series expansions, while the recursive relations of the field solutions between the bottom and top surfaces for any arbitrary multilayers in presence of perfect/imperfect internal interfaces are obtained by means of the dual variable and position technique. Two application examples dealing with graphite fiber/epoxy matrix composites and thermal barrier coated superalloys are exhibited in Section 4.1, and conclusions are drawn in Section 5.

2. The hetero-thermoelastic problem

Figure (1) describes the three-dimensional multilayered system that consists of an arbitrary number of N-bonded orthotropic, dissimilar, linearly thermoelastic, and rectangular layers with fully coupled thermo-mechanical effects. The k^{th} homogeneous layer is surrounded by two internal lower and upper interfaces, located at $z = z_k$ and $z = z_{k+1}$, respectively. The corresponding thickness is $h_k = z_{k+1} - z_k$. A global orthogonal system $(x, y, z) = (x_1, x_2, x_3)$ with Cartesian coordinates is attached to the multilayers where the origin is located at one of the four corners on the bottom surface and all plates are defined in the positive z-region, while the in-plane $x \parallel x_1$- and $y \parallel x_2$- directions are aligned with the horizontal edges to the plate boundaries. It also follows that $z = z_1 = 0$ and $z = z_{N+1} = H$ at the bottom and top surfaces, respectively, where H is the total thickness in the vertical direction of the multilayers. The dimensions in the $x \parallel x_1$- and $y \parallel x_2$- directions are L_x and L_y for all thermoelastic plates, respectively. The four lateral sides are assumed to satisfy the simply supported boundary conditions, and the internal interfaces between two adjacent layers are perfectly or imperfectly connected, which will be discussed later on.

2.1. Governing equations

In the reference state, the body is undeformed and is stress-free at a uniform absolute (reference) temperature T_0 in the absence of external forces. Without considering heat sources in the present context of thermoelasticity theory, the multilayered system undergoes a temperature change field $\theta(x_j,t) = T(x_j,t) - T_0$ in Kelvin (K), accompanying by a deformation state specified by the position- and time-dependent displacement vector $u_i(x_j,t)$, expressed in meter (m). Assuming infinitesimal deformation and temperature changes, the mechanical and thermal properties of the material are considered as constants during deformation and temperature processes since $|\partial u_i(x_j,t)/\partial x_j| \ll 1$ and $|\theta(x_j,t)/T_0| \ll 1$, when the body is subjected to external forces. The constitutive equation for the anisotropic heat conduction problem relates linearly the heat flux vector q_i in W/m^2 to the local temperature gradient, as follows

$$q_i = -k_{ij}\,\theta_{,j}\,, \tag{1}$$

where k_{ij} are the coefficients of thermal conductivity tensor in W/m/K. In eq. (1), a comma followed by index j denotes partial differentiation with respect to the position x_j of a material point with $j = 1,2,3$, and a repeated index implies summation over the range of the index. In the following algebraic manipulation, the flux vector q_i^* is introduced such that $q_i^* = -q_i = k_{ij}\,\theta_{,j}$, with opposite sign according to eq. (1), in order to make carefully use of the mathematically elegant and numerically powerful Stroh formalism. The crucial reason is that the explicit thermoelasticity-based matrix $\mathbf{T}$, provided in the following by eq. (20a), is required to be symmetric and positive definite, as will be made consistent with the Stroh formalism [47–51]. On the other hand, the anisotropic stress-strain constitutive relations for each linear and homogeneous thermoelastic plate including thermal stresses are given by

$$\sigma_{ij} = c_{ijkl}u_{k,l} - \beta_{ij}\theta = c_{ijkl}u_{k,l} - c_{ijkl}\alpha_{kl}\theta\,, \tag{2}$$

where σ_{ij} is the elastic stress tensor in N/m^2, c_{ijkl} are the elastic stiffness constants in N/m^2, and β_{ij} are the thermal constants in N/m^2/K. In general, the coefficients β_{ij} can be obtained in terms of the thermal expansion coefficients α_{kl} in 1/K and the stiffness tensor, as stipulated in eq. (2). For orthotropic materials with the three orthogonal planes of symmetry in the fixed Cartesian coordinates (x_1,x_2,x_3), eq. (2) can be expressed in the matrix form as

$$\begin{bmatrix}\sigma_{11}\\ \sigma_{22}\\ \sigma_{33}\\ \sigma_{23}\\ \sigma_{13}\\ \sigma_{12}\end{bmatrix} = \begin{bmatrix} c_{11} & c_{12} & c_{13} & 0 & 0 & 0\\ c_{12} & c_{22} & c_{23} & 0 & 0 & 0\\ c_{13} & c_{23} & c_{33} & 0 & 0 & 0\\ 0 & 0 & 0 & c_{44} & 0 & 0\\ 0 & 0 & 0 & 0 & c_{55} & 0\\ 0 & 0 & 0 & 0 & 0 & c_{66}\end{bmatrix}\begin{bmatrix} u_{1,1}\\ u_{2,2}\\ u_{3,3}\\ u_{2,3}+u_{3,2}\\ u_{1,3}+u_{3,1}\\ u_{1,2}+u_{2,1}\end{bmatrix} - \begin{bmatrix}\beta_{11}\\ \beta_{22}\\ \beta_{33}\\ 0\\ 0\\ 0\end{bmatrix}\theta\,, \tag{3}$$

with c_{ij} the stiffness tensor indexed in Voigt notation. From thermodynamic theory, the use of the principle of conservation of energy reads [52]

$$q_{i,i}^* = \rho c_p\dot{\theta} + T_0\,\beta_{ii}\dot{u}_{i,i}\,, \tag{4}$$

with ρ the mass density in kg/m^3, c_p the specific heat capacity at constant strain in J/kg/K, and the superposed dot denotes the differentiation with respect to time. Furthermore, the equation of motion for the linear thermoelastic deformations is defined by

$$\sigma_{ij,j} = \rho\ddot{u}_i\,, \tag{5}$$

without body forces acting on the body, in which the thermal effects implicitly arise from the constitutive relation (3). Assuming time-harmonic vibration motion in the present work, the field solution of the elastic displacement vector u_i in eqs. (3) and (5) is sought in the complex standard form and is separated into a function of position and a function of time, as follows

$$u_i(x_1,x_2,z,t) = \hat{u}_i(x_1,x_2,z)\,\mathrm{e}^{i\omega t}\,, \tag{6}$$

where $\hat{u}_i$ is the time-independent displacement vector, ω is the angular vibration frequency of excitation in rad/s, and t is time in s. Substituting separately eq. (6) into eqs. (1) and (2), the nonlinear heat conduction relation and the governing partial differential equation of motion in eq. (4) and (5) read

$$\begin{cases} i\omega\left(\rho c_p \theta + T_0\,\beta_{ii} u_{i,i}\right) - k_{ii}\,\theta_{,ii} = 0\,, & \text{(7a)} \\ \quad \rho\omega^2 u_i + c_{ijkl} u_{k,lj} - \beta_{ii}\theta_{,i} = 0\,, & \text{(7b)} \end{cases}$$

exhibiting the fully coupled displacement-temperature equations of motion and heat conduction. As proposed in the recent uncoupled thermoelastic formulation in Ref. [13], a representation of field solutions by means of double Fourier trigonometric expansions is considered in each layer to solve the three-dimensional time-harmonic system of eqs. (7), as follows

$$\begin{bmatrix} \theta\left(x_1,x_2,z,t\right) \\ q_3\left(x_1,x_2,z,t\right) \end{bmatrix} = \mathrm{e}^{i\omega t} \sum_{m=1}^{\infty}\sum_{n=1}^{\infty} \begin{bmatrix} \bar{\theta}\left(z\right)\sin\left(p_m x_1\right)\sin\left(q_n x_2\right) \\ \bar{q}_3\left(z\right)\sin\left(p_m x_1\right)\sin\left(q_n x_2\right) \end{bmatrix} = \mathrm{e}^{i\omega t}\,\mathrm{e}^{\eta z} \sum_{m=1}^{\infty}\sum_{n=1}^{\infty} \begin{bmatrix} c_T \sin\left(p_m x_1\right)\sin\left(q_n x_2\right) \\ d_T \sin\left(p_m x_1\right)\sin\left(q_n x_2\right) \end{bmatrix}, \tag{8}$$

where η and the expansion coefficients c_T and d_T are to be determined from the boundary conditions at the internal interfaces between adjoining plates, and must satisfy all the prescribed boundary conditions. In eq. (8), the half-wave numbers are given by $p_m = m\pi/L_x$ and $q_n = n\pi/L_y$, with m and n being two positive integers, so that all Fourier series expansion coefficients are related to the summations for m and n. The in-plane and normal flux components of q_i^* are given from eq. (1) by

$$q_1^*\left(x_1,x_2,z,t\right) = k_{11}\,p\,\mathrm{e}^{i\omega t}\,\mathrm{e}^{\eta z} c_T \cos\left(p x_1\right)\sin\left(q x_2\right), \tag{9a}$$

$$q_2^*\left(x_1,x_2,z,t\right) = k_{22}\,q\,\mathrm{e}^{i\omega t}\,\mathrm{e}^{\eta z} c_T \sin\left(p x_1\right)\cos\left(q x_2\right), \tag{9b}$$

$$q_3^*\left(x_1,x_2,z,t\right) = k_{33}\,\eta\,\mathrm{e}^{i\omega t}\,\mathrm{e}^{\eta z} c_T \sin\left(p x_1\right)\sin\left(q x_2\right), \tag{9c}$$

so that c_T is linearly related to d_T by

$$d_T = k_{33}\,\eta\,c_T\,, \tag{10}$$

according to the second relation in eqs. (8) and eq. (9c). In eqs. (9) and in the following, both superscripts over p_m and q_n and both infinite sums as in eqs. (8) are omitted to avoid notational complexity, although whenever the periodic terms $\{p,q\}$ arise, summation over m and n must be made. In virtue of the infinite series expansion in eqs. (8), the elastic displacements, tractions and in-plane stresses are written as follows

$$u_i\left(x_1,x_2,z,t\right) = \mathrm{e}^{i\omega t} \begin{bmatrix} \bar{u}_1(z)\cos\left(p x_1\right)\sin\left(q x_2\right) \\ \bar{u}_2(z)\sin\left(p x_1\right)\cos\left(q x_2\right) \\ \bar{u}_3(z)\sin\left(p x_1\right)\sin\left(q x_2\right) \end{bmatrix} = \mathrm{e}^{i\omega t}\,\mathrm{e}^{\eta z} \begin{bmatrix} a_1\cos\left(p x_1\right)\sin\left(q x_2\right) \\ a_2\sin\left(p x_1\right)\cos\left(q x_2\right) \\ a_3\sin\left(p x_1\right)\sin\left(q x_2\right) \end{bmatrix}, \tag{11a}$$

$$t_i\left(x_1,x_2,z,t\right) = \mathrm{e}^{i\omega t} \begin{bmatrix} \bar{\sigma}_{31}(z)\cos\left(p x_1\right)\sin\left(q x_2\right) \\ \bar{\sigma}_{32}(z)\sin\left(p x_1\right)\cos\left(q x_2\right) \\ \bar{\sigma}_{33}(z)\sin\left(p x_1\right)\sin\left(q x_2\right) \end{bmatrix} = \mathrm{e}^{i\omega t}\,\mathrm{e}^{\eta z} \begin{bmatrix} b_1\cos\left(p x_1\right)\sin\left(q x_2\right) \\ b_2\sin\left(p x_1\right)\cos\left(q x_2\right) \\ b_3\sin\left(p x_1\right)\sin\left(q x_2\right) \end{bmatrix}, \tag{11b}$$

$$\tau_i\left(x_1,x_2,z,t\right) = \mathrm{e}^{i\omega t} \begin{bmatrix} \bar{\sigma}_{11}(z)\sin\left(p x_1\right)\sin\left(q x_2\right) \\ \bar{\sigma}_{12}(z)\cos\left(p x_1\right)\cos\left(q x_2\right) \\ \bar{\sigma}_{22}(z)\sin\left(p x_1\right)\sin\left(q x_2\right) \end{bmatrix} = \mathrm{e}^{i\omega t}\,\mathrm{e}^{\eta z} \begin{bmatrix} c_1\sin\left(p x_1\right)\sin\left(q x_2\right) \\ c_2\cos\left(p x_1\right)\cos\left(q x_2\right) \\ c_3\sin\left(p x_1\right)\sin\left(q x_2\right) \end{bmatrix}, \tag{11c}$$

where a_i, b_i and c_i are complex valued constants to be determined. According to eqs. (11), eq. (3) reads

$$\begin{aligned}
\begin{bmatrix} \tau_1 \\ \tau_3 \\ t_3 \\ t_2 \\ t_1 \\ \tau_2 \end{bmatrix} &= \mathrm{e}^{i\omega t}\,\mathrm{e}^{\eta z} \begin{bmatrix} c_1 \sin(px_1)\sin(qx_2) \\ c_3 \sin(px_1)\sin(qx_2) \\ b_3 \sin(px_1)\sin(qx_2) \\ b_2 \sin(px_1)\cos(qx_2) \\ b_1 \cos(px_1)\sin(qx_2) \\ c_2 \sin(px_1)\cos(qx_2) \end{bmatrix} \\
&= \mathrm{e}^{i\omega t}\,\mathrm{e}^{\eta z} \begin{bmatrix} c_{11} & c_{12} & c_{13} & 0 & 0 & 0 \\ c_{12} & c_{22} & c_{23} & 0 & 0 & 0 \\ c_{13} & c_{23} & c_{33} & 0 & 0 & 0 \\ 0 & 0 & 0 & c_{44} & 0 & 0 \\ 0 & 0 & 0 & 0 & c_{55} & 0 \\ 0 & 0 & 0 & 0 & 0 & c_{66} \end{bmatrix} \begin{bmatrix} -pa_1 \sin(px_1)\sin(qx_2) \\ -qa_2 \sin(px_1)\sin(qx_2) \\ \eta a_3 \sin(px_1)\sin(qx_2) \\ (\eta a_2 + qa_3)\sin(px_1)\cos(qx_2) \\ (\eta a_1 + pa_3)\cos(px_1)\sin(qx_2) \\ (qa_1 + pa_2)\sin(px_1)\cos(qx_2) \end{bmatrix} - \mathrm{e}^{i\omega t}\,\mathrm{e}^{\eta z} \begin{bmatrix} \beta_{11} c_T \sin(px_1)\sin(qx_2) \\ \beta_{22} c_T \sin(px_1)\sin(qx_2) \\ \beta_{33} c_T \sin(px_1)\sin(qx_2) \\ 0 \\ 0 \\ 0 \end{bmatrix},
\end{aligned} \tag{12}$$

which gives rise to the following relations on the unknown expansion coefficients, here between b_i and $[a_i, c_T]^{\mathrm{t}}$ for the normal stress components, i.e.

$$\begin{bmatrix} b_1 \\ b_2 \\ b_3 \end{bmatrix} = \begin{bmatrix} \eta c_{55} & 0 & p c_{55} & 0 \\ 0 & \eta c_{44} & q c_{44} & 0 \\ -p c_{13} & -q c_{23} & \eta c_{33} & -\beta_{33} \end{bmatrix} \begin{bmatrix} a_1 \\ a_2 \\ a_3 \\ c_T \end{bmatrix}, \tag{13}$$

as well as between c_i and $[a_i, c_T]^{\mathrm{t}}$ for the in-plane shear stress components, i.e.

$$\begin{bmatrix} c_1 \\ c_2 \\ c_3 \end{bmatrix} = \begin{bmatrix} -p c_{11} & -q c_{12} & \eta c_{13} & -\beta_{11} \\ q c_{66} & p c_{44} & 0 & 0 \\ -p c_{12} & -q c_{22} & \eta c_{23} & -\beta_{22} \end{bmatrix} \begin{bmatrix} a_1 \\ a_2 \\ a_3 \\ c_T \end{bmatrix}, \tag{14}$$

for which both 3×4 matrices in eqs. (13) and (14) depend on η, p_m and q_n as well as the thermoelastic constants for each homogeneous plate. Combining eqs. (10) and (13), the components that link the displacement/temperature with the normal stress/flux are obtained as follows

$$\begin{bmatrix} b_1 \\ b_2 \\ b_3 \\ d_T \end{bmatrix} = \begin{bmatrix} \eta c_{55} & 0 & p c_{55} & 0 \\ 0 & \eta c_{44} & q c_{44} & 0 \\ -p c_{13} & -q c_{23} & \eta c_{33} & -\beta_{33} \\ 0 & 0 & 0 & \eta k_{33} \end{bmatrix} \begin{bmatrix} a_1 \\ a_2 \\ a_3 \\ c_T \end{bmatrix}, \tag{15}$$

which becomes a fundamental relation in the fully coupled relation between $[b_i, d_T]^{\mathrm{t}}$ and $[a_i, c_T]^{\mathrm{t}}$. Further appropriate relations between a_i and c_T can be derived from eq. (7a), such that

$$c_T\left(-p^2 k_{11} - q^2 k_{22} + \eta^2 k_{33}\right) - i\omega\rho c_p c_T = i\omega T_0\left(-\beta_{11} p a_1 - \beta_{22} q a_2 + \beta_{33}\eta a_3\right), \tag{16}$$

while the equation of time-harmonic motion in eq. (7b) gives

$$p\left(-pc_{11}a_1 - qc_{12}a_2 + \eta c_{13}a_3 - \beta_{11}c_T\right) - c_{66}q\left(qa_1 + pa_2\right) + c_{55}\eta\left(\eta a_1 + pa_3\right) + \rho\omega^2 a_1 = 0\,, \tag{17a}$$

$$-pc_{66}\left(qa_1 + pa_2\right) + q\left(-pc_{12}a_1 - qc_{22}a_2 + \eta c_{23}a_3 - \beta_{22}c_T\right) + c_{44}\eta\left(\eta a_2 + qa_3\right) + \rho\omega^2 a_2 = 0\,, \tag{17b}$$

$$-pc_{55}\left(\eta a_1 + pa_3\right) - qc_{44}\eta\left(\eta a_2 + qa_3\right) + \eta\left(-pc_{13}a_1 - qc_{23}a_2 + \eta c_{33}a_3 - \beta_{33}c_T\right) + \rho\omega^2 a_3 = 0\,, \tag{17c}$$

for which both eqs. (16) and (17) can conveniently be combined and together be recast into a four-dimensional eigenvalue problem, as follows

$$\underbrace{\begin{bmatrix} -p^2c_{11} - q^2c_{66} + \eta^2c_{55} + \rho\omega^2 & -pq\left(c_{12} + c_{66}\right) & p\eta\left(c_{13} + c_{55}\right) & -p\beta_{11} \\ -pq\left(c_{66} + c_{12}\right) & -p^2c_{66} - q^2c_{22} + \eta^2c_{44} + \rho\omega^2 & q\eta\left(c_{23} + c_{44}\right) & -q\beta_{22} \\ -p\eta\left(c_{55} + c_{13}\right) & -q\eta\left(c_{44} + c_{23}\right) & -p^2c_{55} - q^2c_{44} + \eta^2c_{33} + \rho\omega^2 & -\eta\beta_{33} \\ i\omega p\beta_{11}T_0 & i\omega q\beta_{22}T_0 & -i\omega\eta\beta_{33}T_0 & -p^2k_{11} - q^2k_{22} + \eta^2k_{33} + i\rho\omega c_p \end{bmatrix}}_{=\mathbf{N}_{4\times4}} \begin{bmatrix} a_1 \\ a_2 \\ a_3 \\ c_T \end{bmatrix} = \begin{bmatrix} 0 \\ 0 \\ 0 \\ 0 \end{bmatrix} \tag{18}$$

where $\mathbf{N}_{4\times4}$ depends on the vibration frequency ω and the environmental temperature T_0 in addition to p_m, q_n and to the thermoelastic material properties of the plates. Partitioning eq. (15) into two parts, as

$$\boldsymbol{b}_T = \left[\eta\,\mathbf{T} + \mathbf{R}_1\right]\boldsymbol{a}_T\,, \tag{19}$$

with 4×1 vectors $\boldsymbol{a}_T$ and $\boldsymbol{b}_T$ defined by $\boldsymbol{a}_T = [a_i, d_T]^{\mathrm{t}}$ and $\boldsymbol{b}_T = [b_i, d_T]^{\mathrm{t}}$, while $\mathbf{T}$ and $\mathbf{R}_1$ are given by

$$\mathbf{T} = \begin{bmatrix} c_{55} & 0 & 0 & 0 \\ 0 & c_{44} & 0 & 0 \\ 0 & 0 & c_{33} & 0 \\ 0 & 0 & 0 & k_{33} \end{bmatrix}, \tag{20a}$$

$$\mathbf{R}_1 = \begin{bmatrix} 0 & 0 & pc_{55} & 0 \\ 0 & 0 & qc_{44} & 0 \\ -pc_{13} & -qc_{23} & 0 & -\beta_{33} \\ 0 & 0 & 0 & 0 \end{bmatrix}, \tag{20b}$$

and further substituting eq. (19) into eq. (18), a simple quadratic eigenequation with respect to η is obtained, as follows

$$\left[\eta^2\mathbf{T} + \eta\left(\mathbf{R}_1 + \mathbf{R}_2\right) + \mathbf{Q}\right]\boldsymbol{a}_T = \mathbf{0}\,, \tag{21}$$

which resembles in structure to the original Stroh formalism in terms of the double Fourier expansions for three-dimensional problems. In eq. (21), both matrices $\mathbf{R}_2$ and $\mathbf{Q}$ are given by

$$\mathbf{R}_2 = \begin{bmatrix} 0 & 0 & pc_{13} & 0 \\ 0 & 0 & qc_{23} & 0 \\ -pc_{55} & -qc_{44} & 0 & 0 \\ 0 & 0 & -i\omega\beta_{33}T_0 & 0 \end{bmatrix}, \tag{22a}$$

$$\mathbf{Q} = \begin{bmatrix} -p^2c_{11} - q^2c_{66} + \rho\omega^2 & -pq\left(c_{12} + c_{66}\right) & 0 & -p\beta_{11} \\ -pq\left(c_{12} + c_{66}\right) & -p^2c_{66} - q^2c_{22} + \rho\omega^2 & 0 & -q\beta_{22} \\ 0 & 0 & -p^2c_{55} - q^2c_{44} + \rho\omega^2 & 0 \\ i\omega p\beta_{11}T_0 & i\omega q\beta_{22}T_0 & 0 & -p^2k_{11} - q^2k_{22} + i\omega\rho c_p \end{bmatrix}, \tag{22b}$$

which are formulated as function of ω and T_0, in contrast to $\mathbf{T}$ and $\mathbf{R}_1$ in eqs. (20). Finally, both eqs. (19) and (21) can be converted into the following linear eigensystem of equations, i.e.

$$\begin{bmatrix} -\mathbf{T}^{-1}\mathbf{R}_1 & \mathbf{T}^{-1} \\ -\mathbf{Q}+\mathbf{R}_2\mathbf{T}^{-1}\mathbf{R}_1 & -\mathbf{R}_2\mathbf{T}^{-1} \end{bmatrix} \begin{bmatrix} \boldsymbol{a}_T \\ \boldsymbol{b}_T \end{bmatrix} = \eta \begin{bmatrix} \boldsymbol{a}_T \\ \boldsymbol{b}_T \end{bmatrix}, \tag{23}$$

which corresponds to an extension of the pseudo-Stroh formalism for fully coupled thermoelastic problem, where η are the complex valued eigenvalues, while $\boldsymbol{a}_T$ and $\boldsymbol{b}_T$ are the corresponding eigenvectors. The linear pseudo-Stroh eigensystem in eq. (23) is solved for the eight eigenvalues and eigenvectors, which appear in complex conjugate pairs [53] and can be conveniently rearranged such that the four eigenvalues $\{\eta_1, \eta_2, \eta_3, \eta_4\}$ have positive real parts, while the remaining solutions have opposite signs.

2.2. The boundary conditions

In the present boundary-value problem, the appropriate boundary conditions that must be satisfied are those on the external surfaces, i.e., at the edges of the multilayered rectangular plate and both horizontal (bottom and top) surfaces with combined time-harmonic thermal and mechanical aspects, as well as those on the internal interfaces of the multilayered rectangular plates. These boundary conditions are described in the following sections.

2.2.1. External boundary conditions

For the simply supported rectangular composite materials with ideal constraints at the edges, the prescribed boundary conditions at four vertical surface planes are expressed in the physical domain as

$$u_2 = u_3 = \sigma_{11} = \theta = 0\,, \quad \text{at}: \; x_1 = 0, \text{ and } \; x_1 = L_x\,, \tag{24a}$$

$$u_1 = u_3 = \sigma_{22} = \theta = 0\,, \quad \text{at}: \; x_2 = 0, \text{ and } \; x_2 = L_y\,, \tag{24b}$$

for all plates along the entire thickness of the multilayered materials. For free vibration analysis, the boundary conditions are given as traction-free at the bottom and top surfaces of the multilayered structures, while the normal heat flux is arbitrary zero on these boundaries for the thermal conduction conditions, i.e.

$$t_1 = t_2 = t_3 = q_3 = 0\,, \quad \text{at}: \; z = 0\,, \tag{25a}$$

$$t_1 = t_2 = t_3 = q_3 = 0\,, \quad \text{at}: \; z = H\,, \tag{25b}$$

for which the two-dimensional Fourier series ansatz for field solutions given in eqs. (8) and (11) satisfy the homogeneous lateral and external boundary conditions given in eqs. (24) eq. (25), for any m and n occurring as parameters. In terms of the present thermal boundary conditions from eqs. (25), the external surfaces are perfectly insulated, such that no heat can flow through these surfaces as described by the ideal Neumann boundary conditions. Other thermal conditions than the ones in eqs. (25) can straightforwardly be applied, as mixed Dirichlet/Neumann boundary conditions, e.g., $q_3 = 0$ and $\theta = 0$ on the bottom and top surfaces, respectively, or vice versa.

2.2.2. Internal boundary conditions

The traditional boundary condition for mechanically compliant non-ideal interfaces in anisotropic composite laminates, which enables conformability to non-flat and irregularly shaped surfaces to accommodate the residual stresses between two adjacent materials, are formulated as follows

$$[\![\, \sigma_{3j}\,(x_1, x_2, z = z_k, t) \,]\!]^{+}_{-} = \sigma_{3j}\,(x_1, x_2, z = z_k^{+}, t) - \sigma_{3j}\,(x_1, x_2, z = z_k^{-}, t) = 0\,, \tag{26a}$$

$$[\![\, u_j\,(x_1, x_2, z = z_k, t) \,]\!]^{+}_{-} = u_j\,(x_1, x_2, z = z_k^{+}, t) - u_j\,(x_1, x_2, z = z_k^{-}, t) = \alpha_j^{(k)}\,\sigma_{j3}\,(x_1, x_2, z_k, t)\,, \tag{26b}$$

where both superscripts $^+$ and $^-$ denote the limit values from the upper and lower sides of any interface located at $z = z_k$, with $k = 2, \ldots, N$. The mechanical contact feature in eqs. (26) is the general spring-type interface condition where traction is continuous but the elastic displacements experience a jump crossing the interface. The proportional interface coefficients $\alpha_j^{(k)}$ in m^3/N are also designated by interface compliances. In practice, when the latter interface compliances approach zero, the standard condition for ideal mechanical interfaces is verified, while the completely mechanically debonded interfaces are characterized when the interface coefficients tend to infinity. For semi-coherent interfaces heterostructures [54, 55], it is also worth noting that misfit dislocation density-based boundary conditions [56–59] can introduced in place of the phenomenological requirement in eq. (26b) to describe the non-uniform internal structures of imperfect interfaces, which in turn govern interfacial properties such as impurity precipitation, point defect mobility, and shearing resistance. Such boundary conditions dedicated to interface patterning will be therefore incorporated in a follow-up formulation using thermoelasticity theory.

As part of the thermal conduction, two anisotropic boundary conditions are taken into account to represent weakly and highly conducting non-ideal interfaces. For weakly conducting interfaces, the Kapitza model is used to describe a possible interfacial thermal resistance, as follows

$$\left[\!\left[q_3\left(x_1, x_2, z = z_k, t\right) \right]\!\right]_-^+ = q_3\left(x_1, x_2, z = z_k^+, t\right) - q_3\left(x_1, x_2, z = z_k^-, t\right) = 0\,, \tag{27a}$$

$$\left[\!\left[\theta\left(x_1, x_2, z = z_k, t\right) \right]\!\right]_-^+ = \theta\left(x_1, x_2, z = z_k^+, t\right) - \theta\left(x_1, x_2, z = z_k^-, t\right) = -\beta_T^{(k)}\, q_3\left(x_1, x_2, z_k, t\right)\,, \tag{27b}$$

causing a jump in the temperature and thus reduces the effective thermal conductivity of the composite material. In eq. (27b), the adiabatic condition at the contact interfaces is obtained when the non-negative interfacial constant $\beta_T^{(k)}$ in Km^2/W tends to infinity. On the other hand, the boundary conditions for highly conducting imperfect interfaces are written as

$$\left[\!\left[q_3\left(x_1, x_2, z = z_k, t\right) \right]\!\right]_-^+ = q_3\left(x_1, x_2, z = z_k^+, t\right) - q_3\left(x_1, x_2, z = z_k^-, t\right) = \gamma_T^{(k)}\, \nabla_{2\mathrm{D}}^2\, \theta\left(x_1, x_2, z_k, t\right)\,, \tag{28a}$$

$$\left[\!\left[\theta\left(x_1, x_2, z = z_k, t\right) \right]\!\right]_-^+ = \theta\left(x_1, x_2, z = z_k^+, t\right) - \theta\left(x_1, x_2, z = z_k^-, t\right) = 0\,, \tag{28b}$$

where $\nabla_{2\mathrm{D}}^2 = (\partial_{11} + \partial_{22})$ is the surface Laplacian operator and $\gamma_T^{(k)}$ is a non-negative interfacial parameter in W/K, for which the upper material is connected to the adjacent lower material with infinite conductivity if $\gamma_T^{(k)}$ approaches infinity.

For both interfacial heat conditions given in eqs. (27) and (28), the perfect thermal conditions for ideal interfaces are met when $\beta_T^{(k)} = \gamma_T^{(k)} = 0$, exhibiting the continuity of temperature and heat flux at ideal interfaces. Because all aforementioned relations are proportional to the common factor $\mathrm{e}^{i\omega t}$, the above mechanical and thermally internal boundary conditions can conveniently be expressed with respect to time-independent field quantities by omitting the time characteristics in eqs. (26), (27) and (28).

3. General and recursive series solutions

General and exact field solutions for each homogeneous plate are derived using an extension of the Stroh formalism for fully coupled thermoelastic problems in three dimensions. The expressions fulfill exactly both governing equations in terms of Fourier series expansion functions as well as the external and internal boundary conditions previously defined. The determination of the specific transfer matrix between field solutions combined with the dual variable and position technique is used to propagate these solutions recursively through all layers of a given multilayered structure without numerical instability issues, including the mechanical and thermal imperfections at interfaces. In the following, because only the z-dependent field expressions from the former solutions are needed to derive the propagation and imperfect matrices using algebraic manipulations, the sine and cosine functions of x_1 and x_2 as well as the time-dependent factor $\mathrm{e}^{i\omega t}$ are conveniently omitted.

3.1. Field relations for each homogeneous plate

The general solution for the z-dependent coefficients of the following appropriate 4×1 vectors $\bar{\boldsymbol{u}}_{\bar{\theta}} = \left[\bar{\boldsymbol{u}}(z), \bar{\theta}(z)\right]^{\mathrm{t}}$ and $\bar{\boldsymbol{t}}_{\bar{q}} = \left[\bar{\boldsymbol{t}}(z), \bar{q}_3(z)\right]^{\mathrm{t}}$ for each layer k can be expressed in the Fourier-transformed domain as

$$\begin{bmatrix} \bar{\boldsymbol{u}}_{\bar{\theta}}(z) \\ \bar{\boldsymbol{t}}_{\bar{q}}(z) \end{bmatrix} = \begin{bmatrix} \mathbf{A}_{\dagger} & \mathbf{A}_{\dagger\dagger} \\ \mathbf{B}_{\dagger} & \mathbf{B}_{\dagger\dagger} \end{bmatrix} \begin{bmatrix} \langle \mathrm{e}^{\boldsymbol{\eta}_{\dagger} z} \rangle & \mathbf{0}_{4\times 4} \\ \mathbf{0}_{4\times 4} & \langle \mathrm{e}^{\boldsymbol{\eta}_{\dagger\dagger} z} \rangle \end{bmatrix} \begin{bmatrix} \boldsymbol{K}_{\dagger} \\ \boldsymbol{K}_{\dagger\dagger} \end{bmatrix}, \tag{29}$$

where $\boldsymbol{K}_{\dagger}$ and $\boldsymbol{K}_{\dagger\dagger}$ are 4×1 constant vectors to be determined from the thermo-mechanical interface boundary conditions. The eight complex eigenvalues $\boldsymbol{\eta} = \left[\boldsymbol{\eta}_{\dagger}, \boldsymbol{\eta}_{\dagger\dagger}\right]^{\mathrm{t}}$ from the linear eigensystem of equations in eq. (23) and quantities $\boldsymbol{K} = \left[\mathbf{K}_{\dagger}, \mathbf{K}_{\dagger\dagger}\right]^{\mathrm{t}}$ in eq. (29) are ordered as follows

$$\begin{aligned} \boldsymbol{\eta}_{\dagger} &= \left[\eta_1, \eta_2, \eta_3, \eta_4\right]^{\mathrm{t}}, \qquad \boldsymbol{\eta}_{\dagger\dagger} = \left[\eta_5, \eta_6, \eta_7, \eta_8\right]^{\mathrm{t}}, \\ \boldsymbol{K}_{\dagger} &= \left[K_1, K_2, K_3, K_4\right]^{\mathrm{t}}, \quad \boldsymbol{K}_{\dagger\dagger} = \left[K_5, K_6, K_7, K_8\right]^{\mathrm{t}}, \end{aligned} \tag{30}$$

and the corresponding 4×4 submatrices are defined as

$$\begin{aligned} \mathbf{A}_{\dagger} &= \left[\boldsymbol{a}_{T_1}, \boldsymbol{a}_{T_2}, \boldsymbol{a}_{T_3}, \boldsymbol{a}_{T_4}\right], \quad \mathbf{A}_{\dagger\dagger} = \left[\boldsymbol{a}_{T_5}, \boldsymbol{a}_{T_6}, \boldsymbol{a}_{T_7}, \boldsymbol{a}_{T_8}\right], \\ \mathbf{B}_{\dagger} &= \left[\boldsymbol{b}_{T_1}, \boldsymbol{b}_{T_2}, \boldsymbol{b}_{T_3}, \boldsymbol{b}_{T_4}\right], \qquad \mathbf{B}_{\dagger\dagger} = \left[\boldsymbol{b}_{T_5}, \boldsymbol{b}_{T_6}, \boldsymbol{b}_{T_7}, \boldsymbol{b}_{T_8}\right], \end{aligned} \tag{31}$$

such that $\mathbf{A}_{\dagger}$ and $\mathbf{B}_{\dagger}$ are the collections of eigenvectors associated with the first four eigenvalues $\boldsymbol{\eta}_{\dagger}$, while $\mathbf{A}_{\dagger\dagger}$ and $\mathbf{B}_{\dagger\dagger}$ are related to the eigenvectors of the conjugate eigenvalues $\boldsymbol{\eta}_{\dagger\dagger}$. In eq. (29), the z-dependent diagonal and exponential matrices are represented by

$$\langle \mathrm{e}^{\boldsymbol{\eta}_{\dagger} z} \rangle = \mathrm{diag}\left[\mathrm{e}^{\eta_1 z}, \mathrm{e}^{\eta_2 z}, \mathrm{e}^{\eta_3 z}, \mathrm{e}^{\eta_4 z}\right], \quad \langle \mathrm{e}^{\boldsymbol{\eta}_{\dagger\dagger} z} \rangle = \mathrm{diag}\left[\mathrm{e}^{\eta_5 z}, \mathrm{e}^{\eta_6 z}, \mathrm{e}^{\eta_7 z}, \mathrm{e}^{\eta_8 z}\right], \tag{32}$$

which complete the thermoelastic solutions in eq. (29). For the k^{th} homogeneous layer of finite thickness h_k with the lower surface at $z = z_k$ and the upper surface at $z = z_{k+1}$, the transferring relation of thermoelastic field solutions between these two locations, which is conveniently considered in general problems of multilayered system, is given by

$$\begin{bmatrix} \bar{\boldsymbol{u}}_{\bar{\theta}}(z) \\ \bar{\boldsymbol{t}}_{\bar{q}}(z) \end{bmatrix}_{z=z_{k+1}} = \mathbf{P}_k(h_k) \begin{bmatrix} \bar{\boldsymbol{u}}_{\bar{\theta}}(z) \\ \bar{\boldsymbol{t}}_{\bar{q}}(z) \end{bmatrix}_{z=z_k}, \tag{33}$$

where the 8×8 forward transfer matrix $\mathbf{P}_k(h_k)$ is expressed as function of the finite thickness h_k. Using a local material coordinate system that is attached to the individual layer k, where the lower surface is located to $z = z_k = 0$, the vectors $\boldsymbol{K}_{\dagger}$ and $\boldsymbol{K}_{\dagger\dagger}$ can be expressed from eq. (29) as follows

$$\begin{bmatrix} \boldsymbol{K}_{\dagger} \\ \boldsymbol{K}_{\dagger\dagger} \end{bmatrix}_k = \begin{bmatrix} \mathbf{A}_{\dagger} & \mathbf{A}_{\dagger\dagger} \\ \mathbf{B}_{\dagger} & \mathbf{B}_{\dagger\dagger} \end{bmatrix}^{-1} \begin{bmatrix} \bar{\boldsymbol{u}}_{\bar{\theta}}(z) \\ \bar{\boldsymbol{t}}_{\bar{q}}(z) \end{bmatrix}_{z=z_k=0}, \tag{34}$$

while setting $z = z_{k+1} = h_k$ in eq. (29) for the upper surface and then substituting eq. (34) into the subsequent result, the following equation is straightforwardly obtained

$$\begin{bmatrix} \bar{\boldsymbol{u}}_{\bar{\theta}}(z) \\ \bar{\boldsymbol{t}}_{\bar{q}}(z) \end{bmatrix}_{z=z_{k+1}=h_k} = \begin{bmatrix} \mathbf{A}_{\dagger} & \mathbf{A}_{\dagger\dagger} \\ \mathbf{B}_{\dagger} & \mathbf{B}_{\dagger\dagger} \end{bmatrix} \begin{bmatrix} \langle \mathrm{e}^{\boldsymbol{\eta}_{\dagger} h_k} \rangle & \mathbf{0}_{4\times 4} \\ \mathbf{0}_{4\times 4} & \langle \mathrm{e}^{\boldsymbol{\eta}_{\dagger\dagger} h_k} \rangle \end{bmatrix} \begin{bmatrix} \mathbf{A}_{\dagger} & \mathbf{A}_{\dagger\dagger} \\ \mathbf{B}_{\dagger} & \mathbf{B}_{\dagger\dagger} \end{bmatrix}^{-1} \begin{bmatrix} \bar{\boldsymbol{u}}_{\bar{\theta}}(z) \\ \bar{\boldsymbol{t}}_{\bar{q}}(z) \end{bmatrix}_{z=z_k=0}, \tag{35}$$

which is also used to determine the transfer matrix $\mathbf{P}_k(h_k)$ in eq. (34), as follows

$$\mathbf{P}_k(h_k) = \begin{bmatrix} \mathbf{P}_{11} & \mathbf{P}_{12} \\ \mathbf{P}_{21} & \mathbf{P}_{22} \end{bmatrix}_k = \begin{bmatrix} \mathbf{A}_{\dagger} & \mathbf{A}_{\dagger\dagger} \\ \mathbf{B}_{\dagger} & \mathbf{B}_{\dagger\dagger} \end{bmatrix} \begin{bmatrix} \langle \mathrm{e}^{\boldsymbol{\eta}_{\dagger} h_k} \rangle & \mathbf{0}_{4\times 4} \\ \mathbf{0}_{4\times 4} & \langle \mathrm{e}^{\boldsymbol{\eta}_{\dagger\dagger} h_k} \rangle \end{bmatrix} \begin{bmatrix} \mathbf{A}_{\dagger} & \mathbf{A}_{\dagger\dagger} \\ \mathbf{B}_{\dagger} & \mathbf{B}_{\dagger\dagger} \end{bmatrix}^{-1}, \tag{36}$$

where the 4×4 submatrices $\left[\mathbf{P}_{\delta\vartheta}\right]_k$ are individually defined for any homogeneous layer with specific thermoelastic properties as well as the specific thickness of the plate k. Each substantial transfer matrix that is associated with each plate is therefore used to connect the field solutions from the bottom to upper surfaces of the entire multilayered system, formally viewed as an assembly of individual plates with particular boundary conditions between two adjacent plates.

3.2. Recursive field solutions in multilayered plates

By use of eq. (29), the criss-cross field solutions at $z = z_k$ and $z = z_{k+1}$ can be rearranged as follows

$$\begin{aligned}\begin{bmatrix}\bar{\boldsymbol{u}}_{\bar{\theta}}(z_k)\\ \bar{\boldsymbol{t}}_{\bar{q}}(z_{k+1})\end{bmatrix} &= \begin{bmatrix}\mathbf{P}_{11} & \mathbf{0}_{4\times4}\\ -\mathbf{P}_{21} & \mathbf{I}_{4\times4}\end{bmatrix}_k^{-1}\begin{bmatrix}\mathbf{I}_{4\times4} & -\mathbf{P}_{12}\\ \mathbf{0}_{4\times4} & \mathbf{P}_{22}\end{bmatrix}_k\begin{bmatrix}\bar{\boldsymbol{u}}_{\bar{\theta}}(z_{k+1})\\ \bar{\boldsymbol{t}}_{\bar{q}}(z_k)\end{bmatrix}\\ &= \begin{bmatrix}\mathbf{P}_{11}^{-1} & -\mathbf{P}_{11}^{-1}\mathbf{P}_{12}\\ \mathbf{P}_{21}\mathbf{P}_{11}^{-1} & -\mathbf{P}_{21}\mathbf{P}_{11}^{-1}\mathbf{P}_{12}+\mathbf{P}_{22}\end{bmatrix}_k\begin{bmatrix}\bar{\boldsymbol{u}}_{\bar{\theta}}(z_{k+1})\\ \bar{\boldsymbol{t}}_{\bar{q}}(z_k)\end{bmatrix} = \mathbf{V}_{8\times8}^k\begin{bmatrix}\bar{\boldsymbol{u}}_{\bar{\theta}}(z_{k+1})\\ \bar{\boldsymbol{t}}_{\bar{q}}(z_k)\end{bmatrix},\end{aligned} \tag{37}$$

where $\mathbf{V}_{8\times8}^k$ is the dual variable and position matrix with components that are related to the transfer submatrices as follows

$$\begin{aligned}&\mathbf{V}_{11}^k = \left[\mathbf{P}_{11}^{-1}\right]_k, \qquad \mathbf{V}_{12}^k = \left[-\mathbf{P}_{11}^{-1}\mathbf{P}_{12}\right]_k,\\ &\mathbf{V}_{21}^k = \left[\mathbf{P}_{21}\mathbf{P}_{11}^{-1}\right]_k, \quad \mathbf{V}_{22}^k = \left[-\mathbf{P}_{21}\mathbf{P}_{11}^{-1}\mathbf{P}_{12}+\mathbf{P}_{22}\right]_k,\end{aligned} \tag{38}$$

for any plate k bonded by the lower interface at z_k and the upper interface at z_{k+1}. The iterative procedure is established by considering the similar sequence for the adjacent layer $k-1$ bounded by both interfaces at $z = z_{k-1}$ and $z = z_k$, and by making use of the continuity conditions of the expansion coefficients at $z = z_k$. Thus, the recursive relation that propagates the thermoelastic solutions from the bottom interface of $(k-1)^{\text{th}}$ layer and the upper interface of the adjacent k^{th} layer is given by

$$\begin{bmatrix}\bar{\boldsymbol{u}}_{\bar{\theta}}(z_{k-1})\\ \bar{\boldsymbol{t}}_{\bar{q}}(z_{k+1})\end{bmatrix} = \mathbf{V}_{8\times8}^{k-1:k}\begin{bmatrix}\bar{\boldsymbol{u}}_{\bar{\theta}}(z_{k+1})\\ \bar{\boldsymbol{t}}_{\bar{q}}(z_{k-1})\end{bmatrix} = \begin{bmatrix}\mathbf{V}_{11}^{k-1:k} & \mathbf{V}_{12}^{k-1:k}\\ \mathbf{V}_{21}^{k-1:k} & \mathbf{V}_{22}^{k-1:k}\end{bmatrix}\begin{bmatrix}\bar{\boldsymbol{u}}_{\bar{\theta}}(z_{k+1})\\ \bar{\boldsymbol{t}}_{\bar{q}}(z_{k-1})\end{bmatrix}, \tag{39}$$

where the superscripts $^{k-1:k}$ denote the resulting propagation submatrices from the layer $k-1$ to layer k, for any perfect internal interfaces identified by $k = 2, \ldots, N$. The corresponding 4×4 recurrence layer-to-layer submatrices in eq. (39) are defined by

$$\mathbf{V}_{8\times8}^{k-1:k}: \begin{cases}\mathbf{V}_{11}^{k-1:k} = \mathbf{V}_{11}^{k-1}\tilde{\mathbf{V}}_{11}^k + \mathbf{V}_{11}^{k-1}\tilde{\mathbf{V}}_{12}^k\left[\mathbf{I}_{4\times4} - \mathbf{V}_{21}^{k-1}\tilde{\mathbf{V}}_{12}^k\right]^{-1}\mathbf{V}_{21}^{k-1}\tilde{\mathbf{V}}_{11}^k, & \text{(40a)}\\ \mathbf{V}_{12}^{k-1:k} = \mathbf{V}_{12}^{k-1} + \mathbf{V}_{11}^{k-1}\tilde{\mathbf{V}}_{12}^k\left[\mathbf{I}_{4\times4} - \mathbf{V}_{21}^{k-1}\tilde{\mathbf{V}}_{12}^k\right]^{-1}\mathbf{V}_{22}^{k-1}, & \text{(40b)}\\ \mathbf{V}_{21}^{k-1:k} = \tilde{\mathbf{V}}_{21}^k + \tilde{\mathbf{V}}_{22}^k\left[\mathbf{I}_{4\times4} - \mathbf{V}_{21}^{k-1}\tilde{\mathbf{V}}_{12}^k\right]^{-1}\mathbf{V}_{21}^{k-1}\tilde{\mathbf{V}}_{11}^k, & \text{(40c)}\\ \mathbf{V}_{22}^{k-1:k} = \tilde{\mathbf{V}}_{22}^k\left[\mathbf{I}_{4\times4} - \mathbf{V}_{21}^{k-1}\tilde{\mathbf{V}}_{12}^k\right]^{-1}\mathbf{V}_{22}^{k-1}, & \text{(40d)}\end{cases}$$

where the individual elements $\mathbf{V}_{\delta\vartheta}^{k-1}$ are specified by replacing k with $k-1$ in eqs. (38), thus by using the corresponding thickness h_{k-1} in eqs. (36) and the specific thermoelastic properties of the layer $k-1$, while the elements $\tilde{\mathbf{V}}_{\delta\vartheta}^k$ are associated with the k^{th} plate. The superposed tilde is used to account for the interfacial imperfections, conceptually considered as dissimilar layers with infinitely small thicknesses (i.e., $h_k \to 0$). Thus, the layer k corresponds either to a fictitious thin-thickness imperfect interface or a traditional finite-thickness material layer. In a general and concise form, $\tilde{\mathbf{V}}_{\delta\vartheta}^k$ are defined for the former by eqs. (45), which are reduced for the latter to $\tilde{\mathbf{V}}_{\delta\vartheta}^k = \mathbf{V}_{\delta\vartheta}^k$ with a perfectly bonded interface between the adjacent layers $k-1$ and k, as reported in the following section.

3.2.1. Thermo-mechanical properties at internal interfaces

For the general multilayered case in presence of imperfect interfaces, the layer-to-layer eqs. (40) are derived by introducing the 8×8 interfacial material matrix $\mathbf{Z}_k^{\text{int}}$ that characterizes the thermal and mechanical imperfections at a given internal interface at $z = z_k$. Because the discrete imperfect interfaces are conceptually considered as distinct and individual layers with infinitely small thicknesses, a supplementary propagation relation, bounded by two fictitious horizontal surfaces, i.e., between the lower side at $z = z_k^-$ to the upper side at $z = z_k^+$ of the interface is incorporated in eqs. (38). Thus, the lower interface of the layer k with specific thermal and mechanical properties is described by

$$\begin{bmatrix}\bar{\boldsymbol{u}}_{\bar{\theta}}(z_k^-)\\ \bar{\boldsymbol{t}}_{\bar{q}}(z_k^+)\end{bmatrix} = \mathbf{Z}_k^{\text{int}}\begin{bmatrix}\bar{\boldsymbol{u}}_{\bar{\theta}}(z_k^+)\\ \bar{\boldsymbol{t}}_{\bar{q}}(z_k^-)\end{bmatrix}, \tag{41}$$

where the corresponding elements of the interfacial matrix $\mathbf{Z}_k^{\text{int}}$ are given by [13]

$$\mathbf{Z}_k^{\text{int}} = \begin{bmatrix} \mathbf{Z}_{11}^{\text{int}} & \mathbf{Z}_{12}^{\text{int}} \\ \mathbf{Z}_{21}^{\text{int}} & \mathbf{Z}_{22}^{\text{int}} \end{bmatrix}_k = \begin{bmatrix} \mathbf{I}_{4\times4} & -\text{diag}\left[\alpha_1^{(k)}, \alpha_2^{(k)}, \alpha_3^{(k)}, -(1-\lambda)\beta_T^{(k)}\right] \\ \text{diag}\left[0, 0, 0, -\lambda\gamma_T^{(k)}\left(p^2+q^2\right)\right] & \mathbf{I}_{4\times4} \end{bmatrix}, \tag{42}$$

within which the mechanical and thermal interface properties $\alpha_j^{(k)}$, $\beta_T^{(k)}$, and $\gamma_T^{(k)}$ are defined by virtue of eqs. (26b), (27b) and (28a) at $z = z_k$, respectively. In eq. (42), the binary term λ is assigned for weakly conducting interfaces with $\lambda = 0$, while $\lambda = 1$ is related to highly conducting interfaces. According to eq. (37) with eq. (38), the propagation from z_k^+ to z_{k+1} in material layer k is described by

$$\begin{bmatrix} \bar{\boldsymbol{u}}_{\bar{\theta}}(z_k^+) \\ \bar{\boldsymbol{t}}_{\bar{q}}(z_{k+1}) \end{bmatrix} = \begin{bmatrix} \mathbf{V}_{11}^k & \mathbf{V}_{12}^k \\ \mathbf{V}_{21}^k & \mathbf{V}_{22}^k \end{bmatrix} \begin{bmatrix} \bar{\boldsymbol{u}}_{\bar{\theta}}(z_{k+1}) \\ \bar{\boldsymbol{t}}_{\bar{q}}(z_k^+) \end{bmatrix}, \tag{43}$$

so that eqs. (41) and (43) are combined as follows

$$\begin{bmatrix} \bar{\boldsymbol{u}}_{\bar{\theta}}(z_k^-) \\ \bar{\boldsymbol{t}}_{\bar{q}}(z_{k+1}) \end{bmatrix} = \begin{bmatrix} \tilde{\mathbf{V}}_{11}^k & \tilde{\mathbf{V}}_{12}^k \\ \tilde{\mathbf{V}}_{21}^k & \tilde{\mathbf{V}}_{22}^k \end{bmatrix} \begin{bmatrix} \bar{\boldsymbol{u}}_{\bar{\theta}}(z_{k+1}) \\ \bar{\boldsymbol{t}}_{\bar{q}}(z_k^-) \end{bmatrix}, \tag{44}$$

where the corresponding recurrence relations are given by

$$\begin{cases} \tilde{\mathbf{V}}_{11}^k = \mathbf{V}_{11}^k + \mathbf{V}_{11}^k \mathbf{Z}_{12}^{\text{int}}\left[\mathbf{I}_{4\times4} - \mathbf{Z}_{12}^{\text{int}}\mathbf{V}_{21}^k\right]^{-1}\mathbf{V}_{21}^k, & \text{(45a)} \\ \tilde{\mathbf{V}}_{12}^k = \mathbf{V}_{12}^k + \mathbf{V}_{11}^k \mathbf{Z}_{12}^{\text{int}}\left[\mathbf{I}_{4\times4} - \mathbf{Z}_{12}^{\text{int}}\mathbf{V}_{21}^k\right]^{-1}\mathbf{V}_{22}^k, & \text{(45b)} \\ \tilde{\mathbf{V}}_{21}^k = \mathbf{Z}_{21}^{\text{int}} + \left[\mathbf{I}_{4\times4} - \mathbf{Z}_{12}^{\text{int}}\mathbf{V}_{21}^k\right]^{-1}\mathbf{V}_{21}^k, & \text{(45c)} \\ \tilde{\mathbf{V}}_{22}^k = \left[\mathbf{I}_{4\times4} - \mathbf{Z}_{12}^{\text{int}}\mathbf{V}_{21}^k\right]^{-1}\mathbf{V}_{22}^k, & \text{(45d)} \end{cases}$$

completing eqs. (40). It is worth noting that both sets of eqs. (40) and (45) are obviously equivalent in structure, in which the transfer matrices dedicated to layer $k-1$ are replaced with the interfacial submatrices, and that the submatrices $\tilde{\mathbf{V}}_{\delta\vartheta}^k$ in eqs. (45) are reduced to $\mathbf{V}_{\delta\vartheta}^k$ given by eqs. (38) for the perfect interfacial case, thus when the perfect thermoelastic interface conditions are satisfied, i.e., $\alpha_j^{(k)} = \beta_T^{(k)} = \gamma_T^{(k)} = 0$ in eq. (42).

4. Application examples

Illustrative examples of the fully coupled thermoelasticity theory in multilayered structures are provided for free vibration analysis. Two example cases are analyzed and specific effects on the field solutions in modern applications are qualitatively described. Case 1 is related to the free vibration response of a graphite fiber/epoxy matrix composite with high anisotropy for different stacking sequences of symmetric and anti-symmetric cross-ply layups with 0° (i.e., fibers along the x_1 direction) and 90° (i.e., along the x_2 direction) plies. Case 2 illustrates further effects of different interfacial boundary conditions between both ZrO_2 and CMSX4 constituents in thermal barrier coated superalloys on the natural frequencies and vibration mode shapes. The residual stress modal analysis is also investigated for two different environmental temperatures, at $T_0 = 293$ K and $T_0 = 1500$ K. For the second high-temperature application example, the material coefficients of CMSX4 are defined at $T_0 = 1500$ K only, while the material properties of the zirconium dioxide (ceramic) have been chosen equal to the ones at room temperature. The material properties used in these two cases are defined in Table 1, from different references in the open literature. Without loss of generality, since the lowest frequencies are the most important in the free vibration analysis of thermoelastic plates, the following discussions are based on calculations with $m = n = 1$ and $L_x = L_y = L$.

4.1. Free vibration responses

The thermoelastic field solutions can be propagated through all layers from the bottom external surface at $z = z_1 = 0$ to the top surface at $z = z_{N+1} = H$, by continuously transferring eq. (39) from one layer to the adjacent layer and passing all internal interfaces

		case 1	case 2		
Property	unit	graphite/epoxy	ZrO_2	CMSX4	
T_0	K	293	293	293	1500
k_{11}	W/m/K	50.0	1.5	7.0	25.0
k_{22}	W/m/K	0.5	1.5	7.0	25.0
k_{33}	W/m/K	0.5	1.5	7.0	25.0
α_{11}	10^{-6}/K	-2.0	10.0	14.0	20.0
α_{22}	10^{-6}/K	50.0	10.0	14.0	20.0
α_{33}	10^{-6}/K	50.0	10.0	14.0	20.0
c_{11}	GPa	201.55	405.0	174.0	130.5
c_{22}	GPa	9.16	405.0	174.0	130.5
c_{33}	GPa	9.16	405.0	174.0	130.5
c_{12}	GPa	3.10	110.0	97.0	72.75
c_{13}	GPa	3.10	110.0	97.0	72.75
c_{23}	GPa	2.32	110.0	97.0	72.75
c_{44}	GPa	2.20	58.0	112.0	84.0
c_{55}	GPa	5.00	58.0	112.0	84.0
c_{66}	GPa	5.00	58.0	112.0	84.0
ρ	kg/m^3	1575.0	5680.0	8374.0	7898.0
c_p	J/kg/K	687.0	1050.0	397.0	1150.0

Table 1: Constituent thermoelastic properties for an effective graphite fiber/epoxy matrix composite (case 1) and a multilayered thermal barrier on a nickel based superalloy (case 2). The thermal expansion coefficients k_{ii} are in W/m/K, the thermal conductivities α_{ii} in 10^{-6}/K, the elastic stiffness components c_{ij} in GPa, the density ρ in kg/m^3, and the specific heat capacity c_p in J/kg/K. These material properties are defined with respect to two environmental temperatures T_0.

with the corresponding interfacial properties, as follows

$$\begin{bmatrix} \bar{\boldsymbol{u}}_{\bar{\theta}}(0) \\ \bar{\boldsymbol{t}}_{\bar{q}}(H) \end{bmatrix} = \mathbf{V}_{8\times 8}^{1:N} \begin{bmatrix} \bar{\boldsymbol{u}}_{\bar{\theta}}(H) \\ \bar{\boldsymbol{t}}_{\bar{q}}(0) \end{bmatrix} = \begin{bmatrix} \mathbf{V}_{11}^{1:N} & \mathbf{V}_{12}^{1:N} \\ \mathbf{V}_{21}^{1:N} & \mathbf{V}_{22}^{1:N} \end{bmatrix} \begin{bmatrix} \bar{\boldsymbol{u}}_{\bar{\theta}}(H) \\ \bar{\boldsymbol{t}}_{\bar{q}}(0) \end{bmatrix}, \tag{46}$$

where the built-in layer-to-layer submatrices $\mathbf{V}_{\delta\vartheta}^{k-1:k}$ from the layer $k-1$ to layer k with $k = 2, 3, \ldots, N$, are given by eqs. (40) with eqs. (45) for interfacial imperfections. According to the external boundary conditions in terms of the tractions and normal heat flux written in eqs. (25) on both external surfaces, eq. (46) is also reduced to

$$\begin{bmatrix} \bar{\boldsymbol{u}}(0) \\ \bar{\theta}(0) \\ \mathbf{0} \\ 0 \end{bmatrix} = \begin{bmatrix} \mathbf{M}_{11} & \boldsymbol{M}_{12} & \mathbf{M}_{13} & \boldsymbol{M}_{14} \\ \boldsymbol{M}_{21} & M_{22} & \boldsymbol{M}_{23} & M_{24} \\ \mathbf{M}_{31} & \boldsymbol{M}_{32} & \mathbf{M}_{33} & \boldsymbol{M}_{34} \\ \boldsymbol{M}_{41} & M_{42} & \boldsymbol{M}_{43} & M_{44} \end{bmatrix} \begin{bmatrix} \bar{\boldsymbol{u}}(H) \\ \bar{\theta}(H) \\ \mathbf{0} \\ 0 \end{bmatrix}, \tag{47}$$

because $\bar{\boldsymbol{t}}(0) = \bar{\boldsymbol{t}}(H) = \mathbf{0}$ under the traction-free boundary condition, and $\bar{q}(0) = \bar{q}(H) = 0$ for the thermal part by the ideal Neumann boundary conditions. The last two sets of expressions in eq. (47) yield

$$\begin{bmatrix} \mathbf{0} \\ 0 \end{bmatrix} = \begin{bmatrix} \mathbf{M}_{31} & \boldsymbol{M}_{32} \\ \boldsymbol{M}_{41} & M_{42} \end{bmatrix} \begin{bmatrix} \bar{\boldsymbol{u}}(H) \\ \bar{\theta}(H) \end{bmatrix} = \mathbf{V}_{21}^{1:N} \begin{bmatrix} \bar{\boldsymbol{u}}(H) \\ \bar{\theta}(H) \end{bmatrix}, \tag{48}$$

for which the dispersive relation is therefore given by

$$\det\left(\mathbf{V}_{21}^{1:N}\right) = M_{42} \det\left(\mathbf{M}_{31} - M_{42}^{-1} \boldsymbol{M}_{32} \otimes \boldsymbol{M}_{41}\right) = 0, \tag{49}$$

by requiring a nontrivial solution of eq. (48) in terms of $\bar{\boldsymbol{u}}_{\bar{\theta}}(H)$, with $M_{42} \neq 0$ and $\otimes$ the dyadic product between both vectors $\boldsymbol{M}_{32}$ and $\boldsymbol{M}_{41}$. In order to determine the fully coupled thermoelastic solutions $\{\bar{\boldsymbol{u}}_{\bar{\theta}}(z_f), \bar{\boldsymbol{t}}_{\bar{q}}(z_f)\}$ at any field point z_j in layer k, eq. (46) is conveniently split into two equivalent systems that recursively propagate the solutions from $z_1 = 0$ to z_f and also from z_f to $z_{N+1} = H$ to obtain at the following sets of linear equations, i.e.

$$\begin{cases} \begin{bmatrix} \bar{\boldsymbol{u}}_{\bar{\theta}}(0) \\ \bar{\boldsymbol{t}}_{\bar{q}}(z_f) \end{bmatrix} = \begin{bmatrix} \mathbf{V}_{11}^{1:j} & \mathbf{V}_{12}^{1:j} \\ \mathbf{V}_{21}^{1:j} & \mathbf{V}_{22}^{1:j} \end{bmatrix} \begin{bmatrix} \bar{\boldsymbol{u}}_{\bar{\theta}}(z_f) \\ \bar{\boldsymbol{t}}_{\bar{q}}(0) \end{bmatrix}, & \text{(50a)} \\ \begin{bmatrix} \bar{\boldsymbol{u}}_{\bar{\theta}}(z_f) \\ \bar{\boldsymbol{t}}_{\bar{q}}(H) \end{bmatrix} = \begin{bmatrix} \mathbf{V}_{11}^{j:N} & \mathbf{V}_{12}^{j:N} \\ \mathbf{V}_{21}^{j:N} & \mathbf{V}_{22}^{j:N} \end{bmatrix} \begin{bmatrix} \bar{\boldsymbol{u}}_{\bar{\theta}}(H) \\ \bar{\boldsymbol{t}}_{\bar{q}}(z_f) \end{bmatrix}, & \text{(50b)} \end{cases}$$

which can be recast as follows

$$\begin{bmatrix} \mathbf{0}_{4\times 1} \\ \mathbf{0}_{4\times 1} \\ \mathbf{0}_{4\times 1} \end{bmatrix} = \begin{bmatrix} \mathbf{V}_{11}^{1:j} & \mathbf{0}_{4\times 4} & -\mathbf{I}_{4\times 4} & \mathbf{0}_{4\times 4} \\ \mathbf{V}_{21}^{1:j} & -\mathbf{I}_{4\times 4} & \mathbf{0}_{4\times 4} & \mathbf{0}_{4\times 4} \\ -\mathbf{I}_{4\times 4} & \mathbf{V}_{12}^{j:N} & \mathbf{0}_{4\times 4} & \mathbf{V}_{11}^{j:N} \end{bmatrix} \begin{bmatrix} \bar{\boldsymbol{u}}_{\bar{\theta}}(z_f) \\ \bar{\boldsymbol{t}}_{\bar{q}}(z_f) \\ \bar{\boldsymbol{u}}_{\bar{\theta}}(0) \end{bmatrix}, \tag{51}$$

because of the prescribed boundary conditions at both external surfaces, i.e., $\bar{\boldsymbol{t}}_{\bar{q}}(0) = \bar{\boldsymbol{t}}_{\bar{q}}(H) = \mathbf{0}_{4\times 1}$ in eqs. (50). Thus, the natural frequencies are obtained by solving eq. (49), while the first and higher displacement and stress mode shapes for the free vibration characteristics of any thermoelastic multilayers with imperfect interfaces are determined by solving the homogeneous systems in eq. (51) with eqs. (40) and (45).

Before illustrating the dispersion equations for the fully coupled thermoelastic multilayered systems, it is worth noting that a preliminary validation has been carried out to demonstrate the accuracy and efficiency of the present plate formalism in determining the natural frequencies in a homogeneous anisotropic elastic plate, thus by neglecting the thermoelastic coupling effects. The results (not shown here) are in exact agreement within $10^{-7}\%$ deviations with the explicit analytical solutions in Ref. [60] for the simplified cases dedicated to the free vibration responses of homogeneous simply supported rectangular structures.

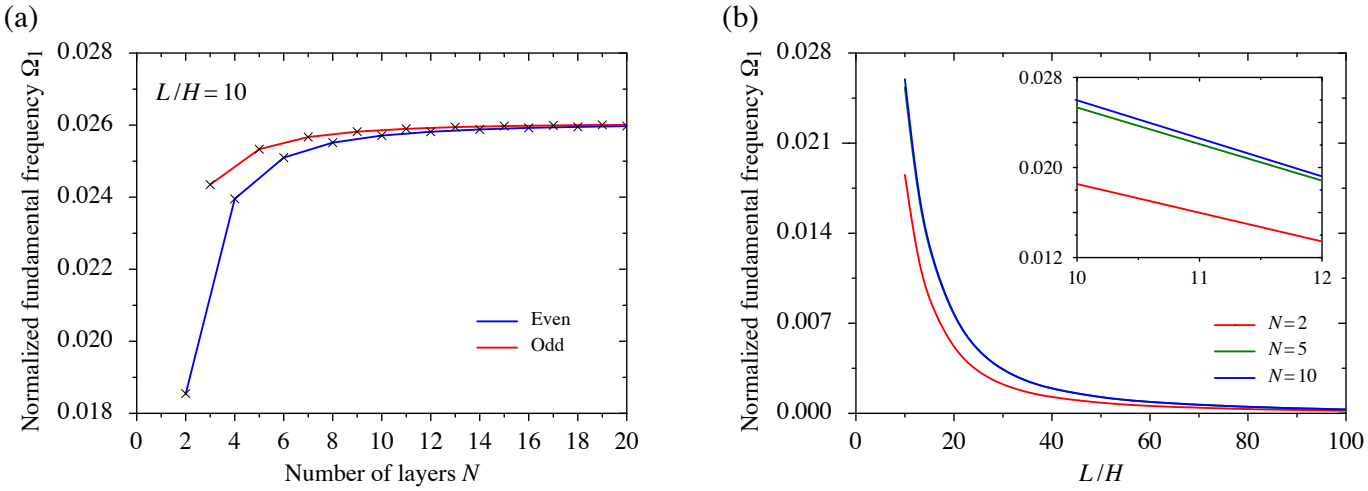

Figure 2: Influence (a) of the number of orthotropic layers N in anti-symmetric (even) and symmetric (odd) cross-ply laminates with $L/H = 10$ and (b) of the length-to-thickness ratio L/H on the normalized natural frequency Ω_1. All rectangular multilayered structures are characterized by the same total thickness H with $L_x = L_y = L$, and the thermoelastic calculations are performed at $T_0 = 293$ K.

4.1.1. Graphite/epoxy cross-ply laminates

The free vibration response of graphite/epoxy fiber-reinforced planar laminated composite materials is presented and discussed for different numbers of thermoelastic plates with orientation and sequence of 0° (i.e., fibers oriented along the x_1 direction) and 90° (i.e., along the x_2 direction) plies with perfectly bonded conditions at interfaces. The calculations are performed at the environmental temperature $T_0 = 293$ K, and the frequencies in the following are normalized as $\Omega = \omega H\sqrt{\rho/c_{11}}$, where the material properties are listed in Table 1. To generalize the results from the graphite/epoxy examples, the dimensions of the rectangular plates are normalized as well, where the lateral dimension L is used to normalize the dimensions of the plates.

Figure (2a) illustrates the effect of the number of orthotropic layers N in anti-symmetric (even) and symmetric (odd) cross-ply laminated structures with $L/H = 10$, while keeping the total thickness H constant for all present multilayered cases. For a low number of layers, the normalized fundamental frequency (i.e., the lowest frequency Ω_1) depends on the anti-symmetric and regular symmetric cross-ply laminations, whereas the fundamental frequency converges to the same natural frequency $\Omega_1^\infty = 0.02597$, when the number of layers increases. Thus, for a large number of thermoelastic plates, i.e., $N \geq 10$ layers, the multilayered systems with harmonic temporal dependence tend to vibrate at a single ply-independent frequency. Figure (2b) shows that the fundamental frequency dramatically decreases with increasing the length-to-thickness ratio L/H for multilayers with 2, 5 and 10 thermoelastic plates. Although large differences in the magnitude of Ω_1 are exhibited between the 2- and 5-layered cases when $L/H \leq 60$, the fundamental frequency tends towards the same single value, i.e., 2×10^{-4}, for very large length-to-thickness ratios of thin-plate multilayers.

Figure (3) displays the first mode shape contours in the (x_1, z)-plane at $x_2/L = 2$ for three layups with 2, 5, and 10 plates, while $L/H = 10$ for these three layered cases. In the plots, the dimensionless quantity $\chi^\#$ is introduced for the different thermoelastic field solutions, such that $\chi^\# = \chi/\max(|\chi|)$ with $\chi = \{\theta, q_3, \sigma_{ij}\}$. It is observed that for different layups, the dimensionless temperature change $\theta^\#$ and normal flux $q_3^\#$ are anti-symmetrically and symmetrically distributed through the thickness z with respect to the median plane at $x_2 = H/2$, depicted by the horizontal dashed lines, respectively. The three residual normal stress components $\sigma_{11}^\#$, $\sigma_{22}^\#$ and $\sigma_{33}^\#$ are differently distributed, for which the latter field $\sigma_{33}^\#$ is anti-symmetric with respect to $x_2 = H/2$, while the amplitude, with positive maximum (negative minimum) value in the middle of the lower (upper) half-space, is roughly three orders of magnitude smaller than the in-plane stress components. The stress concentration of $\sigma_{11}^\#$ is significantly higher in the 0° graphite/epoxy layers than in the 90°-oriented plates, where the fibers are oriented along the x_1 direction, whilst $\sigma_{22}^\#$ leads to the largest concentrations in the 90°-oriented plates with

high stress gradients at the interfaces. The stress repartition in such orthotropic multilayers is also consistent with the rotation of the principal material axes with respect to the global (x_1, x_2, z) coordinates. The von Mises stress field $\sigma^{\#}_{\text{vm}}$, which is a positive definite value, reaches the maximum values on the top surface and the single internal interface for the two-layered structure. The maximum values are located on the bottom and top traction-free surfaces for the 5-layered laminate, while maximum $\sigma^{\#}_{\text{vm}}$ is situated in the second layer from bottom up and on the top surface for the 10-layered structure. Figure (4) depicts from Fig. (3) the through-thickness distribution of the first mode shape at $x_1/L = 2$. Overall, it is shown that the boundary conditions are fully satisfied by the present numerical results, e.g., the traction-free boundary conditions on the bottom and top surfaces for $\sigma^{\#}_{33}$ as well as the continuity of the normal stresses at the internal interfaces. The in-plane stress components are linearly distributed through each individual layer and are discontinuous at the interfaces with large stress gradients. Furthermore, the symmetric profiles of the dimensionless normal flux $q^{\#}_3$ with respect to $z = H/2$ shows that the local peaks of $q^{\#}_3$ are close to the internal interfaces with alternating positive and negative values. This heat flux is zero at the external surfaces, as required by the present adiabatic (perfectly insulated) boundary conditions. It is worth noting that the increase of the number of thermoelastic layers tends to homogenize the free vibration thermal profiles in each plate and to reduce the von Mises stress discontinuities at the interfaces, which is a major cause of fracture and interfacial delamination in multilayered systems.

Figure (5) shows the convergent behaviors for the first three eigenfrequencies with respect to the thin-plate layup numbers, with a higher aspect ratio $L/H = 100$ than the one that depicts the results in Fig. (2a). In particular for the fundamental frequency Ω_1, the thermoelastic coupling decreases when increasing the length-to-thickness ratio. It is also illustrated that the lowest frequency Ω_1 of anti-symmetric (even) and symmetric (odd) cross-ply laminated structures in Fig. (5a) approaches the same "homogenized" plate eigenvalue with increasing the number of layers N, i.e., $\Omega_1 = 0.0003$, more rapidly than the second $\Omega_2 = 0.0222$ and third $\Omega_3 = 0.0241$ eigenfrequencies, where deviations in amplitude for these two last normalized frequencies are still relevant for 20 layers. In other words, the high eigenfrequencies are more sensitive to the different lamination sequences, such that a higher eigenfrequency is recommended to identify or invert the free vibration characteristics of suitable layup features with oriented carbon fibers. Interestingly, the fundamental frequency Ω_1 is (not) dependent on the number of plates with $N \leq 10$ layers with anti-symmetric (symmetric) cross-ply laminates. On the other hand, the second and third natural frequencies do not depend on N with anti-symmetric cross-ply laminates, while Ω_2 (Ω_3) increases (decreases) in amplitude with increasing the number of plates.

Figure (6) displays the mode shape contours for the normalized thermoelastic field quantities of the first three low eigenfrequencies Ω_1, Ω_2, and Ω_3, for which the laminates are regularly symmetric and composed of three layers with $0^\circ/90^\circ/0^\circ$ layups. First, the present formulation predicts the same natural frequencies for the sandwich plates with $0^\circ/90^\circ/0^\circ$ and $90^\circ/0^\circ/90^\circ$ sequences, which remains true for any arbitrary number of layers. From Fig. (6), the following interesting features can be observed: 1. Only the higher eigenmode shapes of the temperature change $\theta^{\#}$ or $q^{\#}_3$ are correlated with the layup of the laminate, since the mode shapes of the fundamental frequency Ω_1 are not; 2. In terms of the residual stress field components, the first and third mode shapes of the in-plane components $\sigma^{\#}_{11}$ and $\sigma^{\#}_{22}$ are undeniably correlated with the lamination scheme of the three-layered composites as well, where $\sigma^{\#}_{33}$ is approximately five orders of magnitude smaller than the in-plane stress components. These complex profiles lead to spatially heterogeneous distribution of the von Mises shear stress $\sigma^{\#}_{\text{vm}}$; 3. The higher eigenmode shapes tend to concentrate the normal heat flux $q^{\#}_3$ at the internal interfaces; 4. The in-plane stress component $\sigma^{\#}_{22}$ ($\sigma^{\#}_{11}$) is considerably larger in magnitude for the eigenfrequency Ω_2 (Ω_3) than for Ω_3 (Ω_2) in the 90° (0°) fiber-oriented plate(s). Figure (7) further shows the mode shape profiles from Fig. (6) along the thickness direction z at $x = L/2$, illustrating the field correlations between the mode shapes and layups of the three-layered laminates. These features indicate that the through-thickness amplitude is extremely dependent on the mode shapes, while only certain of them can be applied to invert the layup structures of the involved laminate. The temperature change $\theta^{\#}$ is roughly zero at the interfaces for Ω_2 and Ω_3 with steep local profiles, which are responsible to the heterogeneous distribution of the normal heat flux profiles. Depending on the natural eigenfrequencies, the compressive or tensile stress components can change in sign, which also alter the residual von Mises stress magnitudes from layer to

layer in the laminated structures.

4.1.2. Thermal barrier coated superalloys

The free vibration analysis on a thermal barrier coated superalloy made of two anisotropic plates, namely the zirconium dioxide (ceramic) ZrO_2 coated Ni-based single crystal superalloy CMSX4, is investigated under two environmental temperatures $T_0 = 293$ K and $T_0 = 1500$ K, for which the material properties are specified in Table 1. Furthermore, both mechanically and thermally (weakly conducting) imperfections at the internal ZrO_2/CMSX4 interfaces are included to describe the effect of imperfect interfaces in the free vibration responses, where the thickness of each plate are $h_{ZrO_2} = 100$ μm and $h_{CMSX4} = 500$ μm. As a preliminary study, the real fundamental frequency ω of the superalloy specimens at $T_0 = 293$ K without any thermal barrier coatings is $\omega_1 = 5469.54$ rad/s, while the frequency increases to $\omega_1 = 7249.62$ rad/s by including the 100 μm-thickness ceramic coating. Overall, the fundamental frequency varies linearly with h_{ZrO_2}. At $T_0 = 1500$ K, the thermal barrier coated system yields $\omega_1 = 6787.52$ rad/s, such that the fundamental frequency ω_1 decreases with increasing the environmental temperature and the latter has a more significant effect on the higher frequencies than that for the lower (not shown here).

Figure (8) illustrates the influence of environmental temperature T_0 as well as the structurally interfacial imperfection on the free vibration characteristics. The variation of the normalized fundamental frequency of the two-layered plate with respect to the isotropic interfacial spring-like stiffness components α_j with $j = \{1,2,3\}$ under both environmental temperature is shown in Fig. (8a). Here, the fundamental frequencies are normalized as $\underline{\Omega}_1 = \omega_1/\omega_1^0$, where ω_1^0 correspond to the case with perfectly bonded conditions with $\alpha_j = 0$ at the ZrO_2/CMSX4 interfaces. Three features are found: 1. The fundamental frequencies decrease with increasing the severity of imperfection at both room and high environmental temperatures; 2. The environmental temperature has more impact on the bilayers with imperfect mechanical contact properties than the perfect interfacial case; 3 For a given imperfect interface (i.e., with given interface stiffness at the contact interface), a higher environmental temperature would correspond to a lower natural frequency. Figures (8b−d) depict the three-dimensional mode shapes for the normalized displacement $u_1^{\#}$, in-plane shear stress $\sigma_{12}^{\#}$, and von Mises stress $\sigma_{\text{vm}}^{\#}$. While label A is for the mode shape with perfect interface under high temperature $T_0 = 1500$ K, label B is related to the mode shape with imperfect interface, i.e., $\alpha_j = 0.1$, under the same thermal environment. It is displayed from these three-dimensional figures that under a high environmental temperature with large interface stiffnesses, the signature mode shapes can operationally be enhanced with much apparent deformation shapes and patterns, as compared to label A.

Figure (9) shows the mode shape variation of the fundamental frequency $\underline{\Omega}_1$ in the thickness direction for different normalized field solutions under different imperfect interface conditions, namely the influence of the structural boundary conditions with different values of α_j in mm^3/N is illustrated in Figs. (9a) and (9b) at $T_0 = 293$ K and $T_0 = 1500$ K, respectively, while the influence of the thermally weakly conducting interfaces at high temperature is depicted in Fig. (9c) by varying the Kapitza parameter β_T in Km^2/W. For comparison between the various cases, these field quantities are normalized by the corresponding maximum values in the considered application samples. For instance, in the middle column, the temperature change is normalized by the maximum among all the different interface stiffness cases, while the in-plane stress field $\sigma_{11}^{\#}$ is normalized by the maximum among all the different interface stiffness cases and among all the stress components. These figures indicate that with increasing interface parameters, the modal feature of the field quantities is significantly altered, in terms of both shapes and magnitudes. Furthermore, with increasing interface parameter, the discontinuity in the in-plane stresses (including also the von Mises stress field) increase. In contrast to the calculations at room temperature, the structural coefficients α_j might have strong effects at high temperature on the thermal quantities $\theta^{\#}$ and $q_3^{\#}$. In particular, the normal heat flux at the ZrO_2/CMSX4 interface that increases with increasing the amplitude of α_j, where a complete reversal variation of $q_3^{\#}$ (green curve) in comparison with lower values (e.g., red and blue curves) is observed close to the internal interface. Since the mode shape is the fundamental feature in the free vibration analysis of multilayered composites, these trends and investigations are useful in inverting interface structures in layered composites. More particularly, for any interfaces that are partially delaminated (adiabatic) the magnitude

of the von Mises stress field $\sigma_{\rm vm}^{\#}$ decreases from $\alpha_j = 0$ to 0.1 Km^2/W (increases from $\beta_T = 0$ to 10^{-5} Km^2/W) in the entire thermal barrier coated superalloys.

5. Concluding remarks

Exact solutions for the free vibration response of three-dimensional, anisotropic, simply supported and multilayered composites with imperfect interfaces have been derived using the fully coupled thermoelasticity theory. For each homogeneous layer in thermal environment, the general field expression of the temperature, heat flux, displacement and stress components is formulated in terms of double Fourier series expansions, which gives rise to a simple and elegant extension of the Stroh formalism including thermomechanical coupling effects. Using the specific conditions at the internal interfaces between adjacent layers, the complete time-harmonic solutions in the multilayered structure is obtained by combining the modified dual variable and position technique with explicit layer-to-layer transfer matrices. The present framework admits different mechanical and thermal boundary conditions to take into account interfacial imperfections, and can be applied to thick and thin laminated structures, without producing numerical instability issue from high frequency and/or large wavenumber.

Results are presented for two application examples, namely the graphite/epoxy cross-ply composites and the thermal barrier coatings on superalloys, for which effects such as stacking lamination sequence, length-to-thickness ratio and the interfacial conditions on the natural frequencies and first and higher vibration mode shapes are deeply investigated. The calculations reveal that the natural frequencies and first and higher vibration mode shapes of the multilayered structures can be considerably affected by increasing the environmental temperature as well as the thermal and mechanical severity of the interfacial imperfections. From these numerical results, the following main features and conclusions can be drawn:

1. The value of the fundamental frequency increases with increasing plate thickness, while the natural frequencies in the graphite/epoxy cross-ply laminates are independent of the lamination sequence in multilayers with the same number of alternating thermoelastic layers,

2. The first three natural frequencies of the cross-ply composites converge to single values with increasing number of layers, which depend significantly on the anti-symmetrically and symmetrically distributed stacking sequence,

3. In contrast with the fundamental frequency, only the higher eigenmode shapes of the temperature change and the heat flux are correlated with the layup of the laminate, where the latter is strongly concentrated at the internal interfaces,

4. In the two-constituent thermal barrier coated superalloys, the natural frequencies increase as the thickness of ceramic increases, while the fundamental frequencies decrease with increasing the spring-like stiffness properties of the imperfect interface at both room and high environmental temperatures,

5. The vibration signature region in the thermal barrier coated superalloys has much apparent deformation shapes and patterns at high temperature with partially delaminated (i.e., with interfacial damage) interfaces than the equivalent samples at room temperature with perfectly bonded conditions,

6. For imperfect interfaces that are partially delaminated, the magnitude of the von Mises stress mode shapes decreases in the entire thermal barrier coated superalloys, while its magnitude increases in presence of partially insulated (i.e., with interfacial thermal resistance) interfaces,

7. The numerous through-thickness stress distributions in 2, 5, and 10 layered composites are intimately correlated to the layups with perfect/imperfect interfaces, so that modal stress analysis as experienced in the present investigations could be exploited to locate the fatigue hotspots in dynamic structures and to guide the structural design of aircraft and spacecraft composite laminates subjected to residual vibrations in the context of reverse interfacial engineering.

Extensions of the formalism to modern free vibration problems as well as buckling [61] and bending [62] analysis of metallic multilayered structures are also possible. For instance, the time-harmonic interactions between semicoherent heterophase interfaces

with core-spreading dislocation structures [63] with extrinsic dislocation loops [64] and interfacial cracks [65, 66] in multifunctional composites would be of great importance to understand their effects on the natural frequencies and lower and higher thermoelastic mode shapes for future renewable energy devices in aerospace structures [67]. Due to the present versatile formalism to take care of imperfect interfaces, other interfacial considerations as the elastic-slip interface model [68, 69] and surface/interface model [70] raised by Gurtin and Murdoch [71] can be introduced for appropriate applications, as well as nonlocal size effects [13] in nano- and micro-scale structures.

References

[1] Padture NP. Advanced structural ceramics in aerospace propulsion. Nat Mater 2016; 15:804-809.

[2] Padture NP. Environmental degradation of high-temperature protective coatings for ceramic-matrix composites in gas-turbine engines. npj Mater Degrad 2019; 3:1-11.

[3] Duhamel JMC. Second mémoire sur les phénomènes thermo-mécaniques. J Ecole Polytechnique 1837; 15:1-57. 1e57.

[4] Biot MA. Thermoelasticity and irreversible thermodynamics. J Appl Phys 1956; 27:240-253.

[5] Nowinski W. Problems of thermoelasticity. Prog Aerosp Sci 1970; 10:1-63.

[6] Hetnarski RB, Ignaczak J. Thermal stress − Advanced theory and applications. Springer: New York 2009.

[7] Tauchert TR. Thermal shock of orthotropic rectangular plates. J Thermal Stresses 1989; 12:241-258.

[8] Vel SS, Batra RC. Exact solution for thermoelastic deformations of functionally graded thick rectangular plates. AIAA J 2002; 40:1421-1433.

[9] Pelletier JL, Vel SS. An exact solution for the steady-state thermoelastic response of functionally graded orthotropic cylindrical shells. Int J Solids Struct 2006; 46:1131-1158.

[10] Vel SS, Batra RC. Three-dimensional analysis of transient thermal stresses in functionally graded plates. Int J Solids Struct 2003; 40:7181-7196.

[11] Wang X, Pan E. Exact solutions for simply supported and multilayered piezothermo-elastic plates with imperfect interfaces. Open Mech J 2007; 1:1-10.

[12] Yang L, Li Y, Gao Y, Pan E. Three-dimensional exact thermo-elastic analysis of multilayered two-dimensional quasicrystal nanoplates. Appl Math Model 2018; 63:203-218.

[13] Vattré A, Pan E. Thermoelasticity of multilayered plates with imperfect interfaces. Accepted to Int J Eng Sci. 2020.

[14] Woo J, Meguid SA. Nonlinear analysis of functionally graded plates and shallow shells. Int J Solids Struct 2001; 38:7409-7421.

[15] Shen HS. Nonlinear bending response of functionally graded plates subjected to transverse loads and in thermal environments. Int J Mech Sci 2002; 44:561-584.

[16] Yang J, Shen HS. Vibration characteristics and transient response of shear-deformable functionally graded plates in thermal environments. J Sound Vib 2002; 255:579-602.

[17] Kim YW. Temperature dependent vibration analysis of functionally graded rectangular plates. J Sound Vib 2005; 284:531-549.

[18] Frostig Y, Thomsen OT. On the free vibration of sandwich panels with a transversely flexible and temperature-dependent core material − Part I: Mathematical formulation. Compos Sci Technol 2009; 69:856-862.

[19] Fazzolari Z, Carrera E. Accurate free vibration analysis of thermo-mechanically pre/post-buckled anisotropic multilayered plates based on a refined hierarchical trigonometric Ritz formulation. Compos Struct 2013; 95:381-402.

[20] Fazzolari Z, Carrera E. Free vibration analysis of sandwich plates with anisotropic face sheets in thermal environment by using the hierarchical trigonometric Ritz formulation. Composites Part B 2013; 50:67-81.

[21] Lee DM, Lee I. Vibration behaviors of thermally postbuckled anisotropic plates using first-order shear deformable plate theory. Comput Struct 1997; 63:371-378.

[22] Praveen GN, Reddy JN. Nonlinear transient thermoelastic analysis of functionally graded ceramic-metal plates. Int J Solids Struct 1998; 33:4457-4476.

[23] Shiau1 LC, Kuo SY. Free vibration of thermally buckled composite sandwich plates. J Vib Acoust 2006; 128:1-7.

[24] Singhaa MK, Ramachandrab LS, Bandyopadhyayb JN. Vibration behavior of thermally stressed composite skew plate. J Sound Vib 2006; 296:1093-1102.

[25] Tran TQN, Lee HP, Lim SP. Structural intensity analysis of thin laminated composite plates subjected to thermally induced vibration. Compos Struct 2007; 78:70-83.

[26] Jeyaraj P, Padmanabhan C, Ganesan N. Vibration and acoustic response of an isotropic plate in a thermal environment. J Vib Acoust 2008; 130:1-6.

[27] Kozlov VI. Thermoelastic vibrations of a rectangular plate. Prikl Mech 1972; 8:123-127.

[28] Reddy JN, Chin CD. Thermomechanical analysis of functionally graded cylinders and plates. J Thermal Stresses 1998; 21:593-626.

[29] Sharma JN. Three-dimensional vibration analysis of a homogeneous transversely isotropic thermoelastic cylindrical panel. J Acoust Soc Am 2001; 110:254-259.

[30] Das NC, Das SN, Das B. Eigenvalue approach to thermoelasticity. J Thermal Stresses 1983; 6:35-43.

[31] Brischetto S, Carrera E. Coupled thermo-mechanical analysis of one-layered and multilayered plates. Compos Struct 2010; 92:1793-1812.

[32] Cho M, Oh J. Higher order zig-zag theory for fully coupled thermo-electric–mechanical smart composite plates. Int J Solids Struct 2004; 41:1331-1356.

[33] Fazzolari FA, Carrera E. Coupled thermoelastic effect in free vibration analysis of anisotropic multilayered plates and FGM plates by using a variable-kinematics Ritz formulation. Eur J Mech A/Solids 2014; 44:157-174.

[34] Cannarozzi AA, Ubertini F. A mixed variational method for linear coupled thermoelastic analysis. Int J Solids Struct 2001; 38:717-739.

[35] Eskandari-Ghadi M, Sture S., Rahimian M. Forati M. Thermoelastodynamics with scalar potential functions. J Eng Mech 2014; 140:54-81.

[36] He H, He C, Chen W, Chen G. Free vibration solution of thick plate by using three-dimensional coupled thermoelastic theory. J Vibroeng 2016; 18:5306-5320.

[37] Hayati Y, Eskandari-Ghadi M. Three-dimensional coupled thermoelastodynamic stress and flux induced wave propagation for isotropic half-space with scalar potential functions. Z Angew Math Phys 2018; 69:1-32.

[38] Burlayenko VN, Sadowski T, Dimitrova S. Three-dimensional free vibration analysis of thermally loaded FGM sandwich plates. Materials 2019; 12:1-21.

[39] Rokhlin, SI, Huang W. Ultrasonic wave interaction with a thin anisotropic layer between two anisotropic solids: exact and asymptotic-boundary-condition methods. J Acoust Soc Am 1992; 92:1729:1742.

[40] Zhou ZD, Yang FP, Kuang ZB. Reflection and transmission of plane waves at the interface of pyroelectric bi-materials. J Sound Vib 2012; 331:3558-3566.

[41] Liu H, Pan E. Time-harmonic loading over transversely isotropic and layered elastic half- spaces with imperfect interfaces. Soil Dyn Earthq Eng 2018; 107:35-47.

[42] Kapitza PL. Collected papers of PL Kapitza. Pergamon Press: Oxford 1965.

[43] Benveniste Y, Miloh T. The effective conductivity of composite with imperfect contact at constituent interfaces. Int J Engng Sci 1986; 24:1537-1552.

[44] Benveniste Y. On the decay of end effects in conduction phenomena: a sandwich strip with imperfect interfaces of low or high conductivity. J Appl Phys 1999; 86:1273-1279.

[45] Benveniste Y. A general interface model for a three-dimensional curved thin anisotropic interphase between two anisotropic media. J Mech Phys Solids 2006; 54:708-734.

[46] Pan E. Green's functions for geophysics: a review. Rep Prog Phys 2019; 82:106801.

[47] Stroh AN. Dislocations and Cracks in Anisotropic Elasticity. Philos Mag 1958; 3:625-646.

[48] Stroh AN. Steady state problems in anisotropic elasticity. J Math Phys 1962; 41:77-103.

[49] Ting TCT. Anisotropic elasticity: theory and applications. Oxford University Press: New York/Oxford 1996.

[50] Pan E, Chen W. Static Green's functions in anisotropic media. Cambridge University Press 2015.

[51] Vattré A, Pan E. Three-dimensional interaction and movements of various dislocations in anisotropic bicrystals with semicoherent interfaces. J Mech Phys Solids 2018; 124:929-956.

[52] Boley BA, Weiner J. Theory of thermal stresses. Wiley: London 1960.

[53] Eshelby J, Read W, Shockley W. Anisotropic elasticity with applications to dislocation theory. Acta Metall 1953; 1:251-259.

[54] Hirth JP, Lothe J. Theory of dislocations. 2nd ed Kriger: Melbourne 1992.

[55] Sutton AP, Balluffi RW. Interfaces in crystalline Materials. Oxford University Press: Oxford 1995.

[56] Vattré A. Mechanical interactions between semicoherent heterophase interfaces and free surfaces in crystalline bilayers. Acta Mater 2015; 93:46-59.

[57] Vattré A. Elastic interactions between interface dislocations and internal stresses in finite-thickness nanolayered materials. Acta Mater 2016; 114:84-197.

[58] Vattré A. Elastic strain relaxation in interfacial dislocation patterns: I. A parametric energy-based framework. J Mech Phys Solids 2017; 105:254-282.

[59] Vattré A. Elastic strain relaxation in interfacial dislocation patterns: II. From long- and short-range interactions to local reactions. J Mech Phys Solids 2017; 105:283-305.

[60] Srinivas S, Rao AK. Bending, vibration and buckling of simply supported thick orthotropic rectangular plates and laminates. Int J Solids Struct 1970; 6:1463-1481.

[61] Yang J, Wu H, Kitipornchai S. Buckling and postbuckling of functionally graded multilayer graphene platelet-reinforced composite beams. Compos Struct 2017; 161:111-118.

[62] Liu D, Li Z, Kitipornchai S, Yang J. Three-dimensional free vibration and bending analyses of functionally graded graphene nanoplatelets-reinforced nanocomposite annular plates. Compos Struct 2019; 229:111453.

[63] Vattré A. Semicoherent heterophase interfaces with core-spreading dislocation structures in magneto-electro-elastic multilayers under external surface loads. J Mech Phys Solids 2019; 124:929-956.

[64] Yuan JH, Huang Y, Chen WQ, Pan E, Kang GZ. Theory of dislocation loops in multilayered anisotropic solids with magneto-electro-elastic couplings. J Mech Phys Solids 2019; 125:440-471.

[65] Saeedi N, Sab K, Caron JF. Delaminated multilayered plates under uniaxial extension. Part I: Analytical analysis using a layerwise stress approach. Int J Solids Struct 2012; 49:3711-3726.

[66] Khanna K, Kotousov A. The stress field due to an interfacial edge dislocation in a multi-layered medium. Int J Solids Struct 2015; 72:1-10.

[67] Adam TJ, Liao G, Peterson J, Geier S, Finke B, Wierach P, Kwade A, Wiedemann M. Multifunctional composites for future energy storage in aerospace structures. Energies 2018; 11:1-21.

[68] Fang XQ, Zhang TF, Li BL, Yuan RJ, Elastic-slip interface effect on dynamic stress around twin tunnels in soil medium subjected to blast waves. Comput Geotech 2019; 119:103301.

[69] Li BL, Fang XQ, Zhang TF, Yang SP. Elastic-slip interface effect on dynamic response of underwater convey tunnel in saturated poroelastic soil subjected to plane waves. Tunn Undergr Space Technol 2020; 103:103468.

[70] Zhu CS, Fang XQ, Liu JX, Li HY. Surface energy effect on nonlinear free vibration behavior of orthotropic piezoelectric cylindrical nano-shells. Eur J Mech A/Solids 2017; 66:423-432.

[71] Gurtin ME., Murdoch AI. A continuum theory of elastic material surfaces. Arch Ration Mech An 1975; 57:291-323.

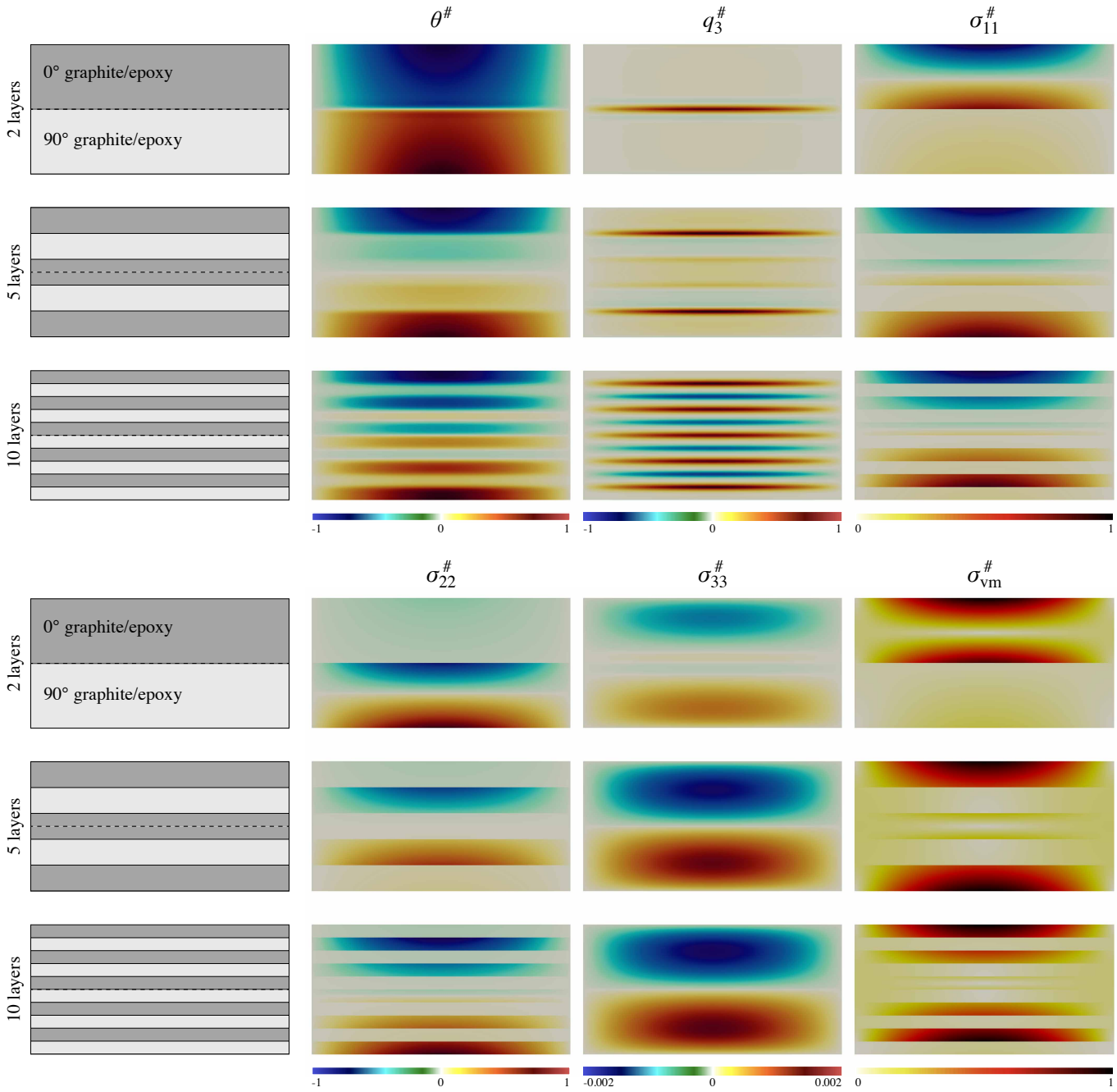

Figure 3: Free vibration distributions of the first mode shape for three multilayered laminates made of 2, 5, and 10 graphite/epoxy plates, namely the dimensionless temperature change $\theta^{\#}$, normal flux $q_3^{\#}$, stress components $\sigma_{ii}^{\#}$, and von Mises stress $\sigma_{\mathrm{vm}}^{\#}$. These three heterosystems with lamination scheme on the left-hand side are described by the same total thickness H with $L_x = L_y$.

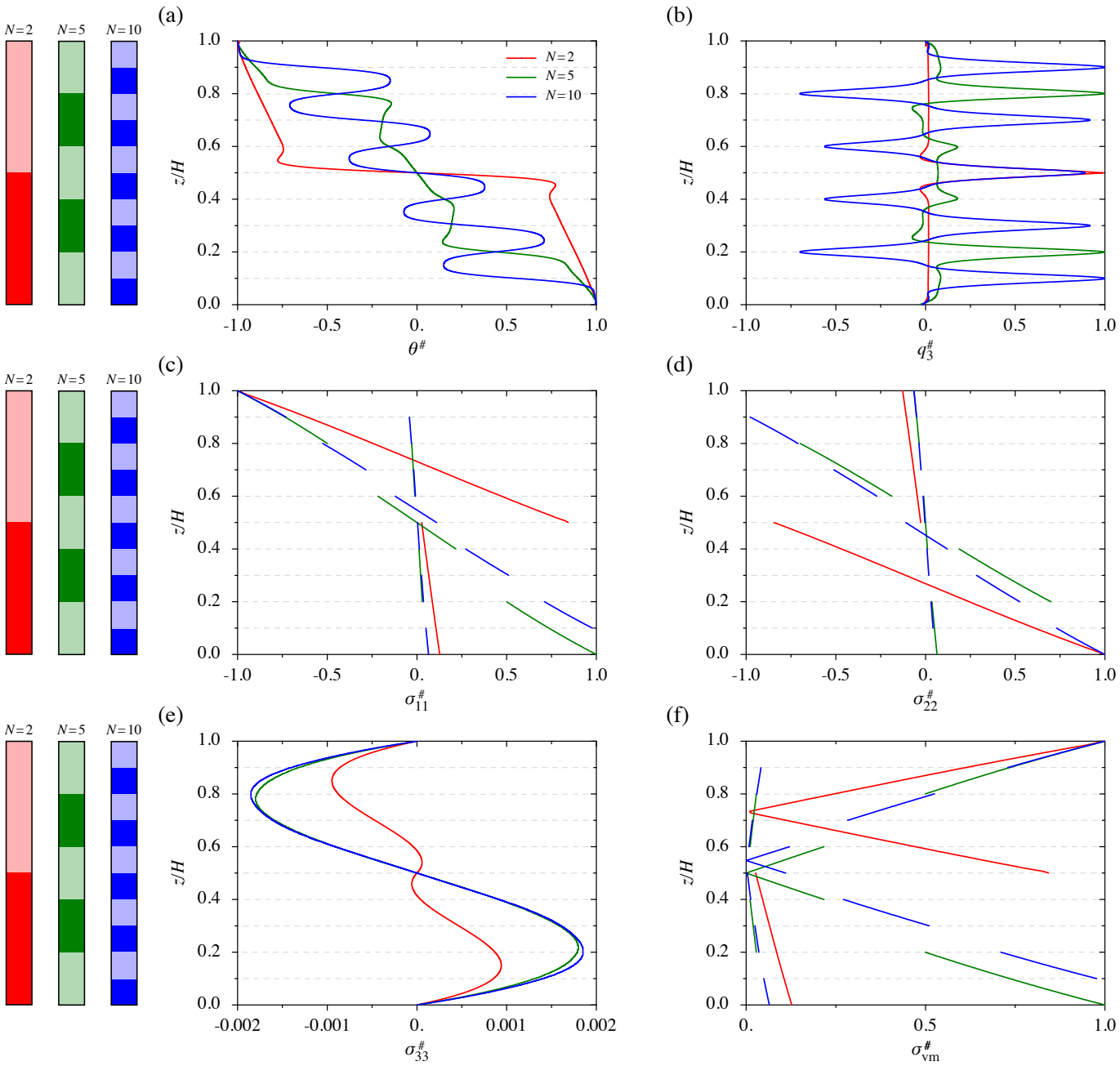

Figure 4: Through-thickness profiles of the first mode shape in the three multilayered systems described in Fig. (3) at $x = L/2$, namely the dimensionless (a) temperature change $\theta^{\#}$, (b) normal flux $q_3^{\#}$, (c-d-e) stress components $\sigma_{ii}^{\#}$, and (f) von Mises stress $\sigma_{\mathrm{vm}}^{\#}$. The dotted horizontal lines correspond to the location of perfect internal interfaces, for which the density depends on the considered case with $N = 2$, 5, and 10 in red, green, and blue, respectively.

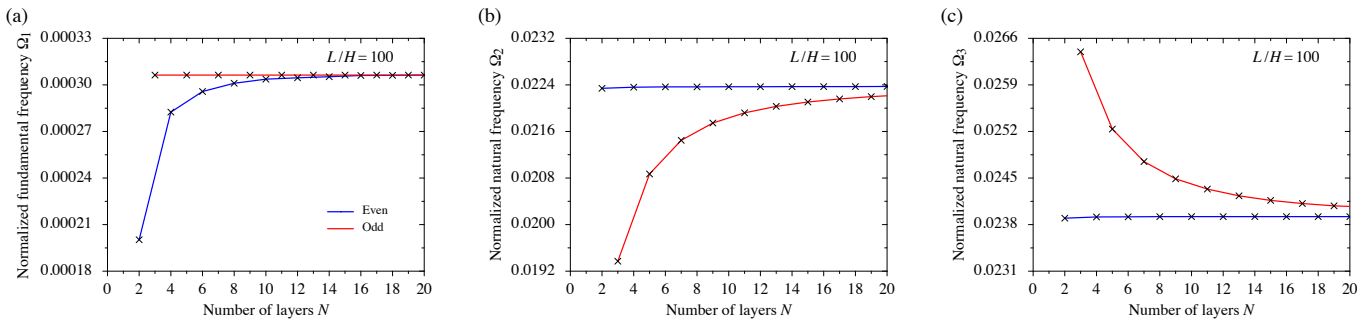

Figure 5: Influence of the number of orthotropic thermoelastic layers N in thin-plate laminate with $L/H = 100$ for the first three normalized frequencies (a) Ω_1, (b) Ω_2, and (c) Ω_3 at $T_0 = 293$ K. The blue and red curves are related to the heterosystems with anti-symmetric (even) and symmetric (odd) cross-ply laminates, respectively.

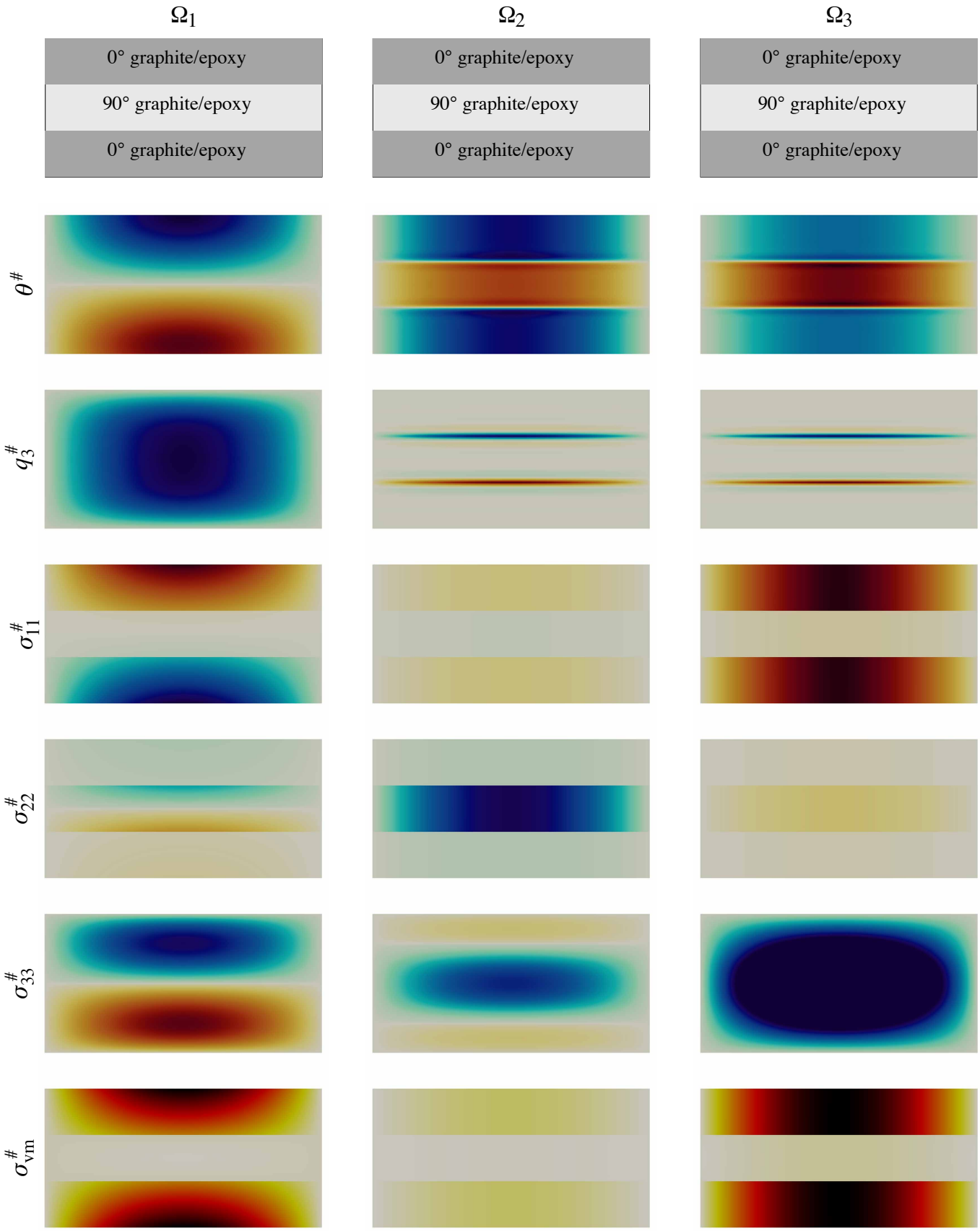

Figure 6: Free vibration distributions of the first three mode shapes Ω_1, Ω_2, and Ω_3 for the symmetric three-layered laminates with $0^\circ/90^\circ/0^\circ$ graphite/epoxy lamination scheme with $L/H = 100$, namely the dimensionless temperature change $\theta^{\#}$, normal flux $q_3^{\#}$, stress components $\sigma_{ii}^{\#}$, and von Mises stress $\sigma_{\mathrm{vm}}^{\#}$. The legends are the same as in Fig. (3), except for $\sigma_{33}^{\#}$ whose the limits are $\pm 2 \times 10^{-5}$.

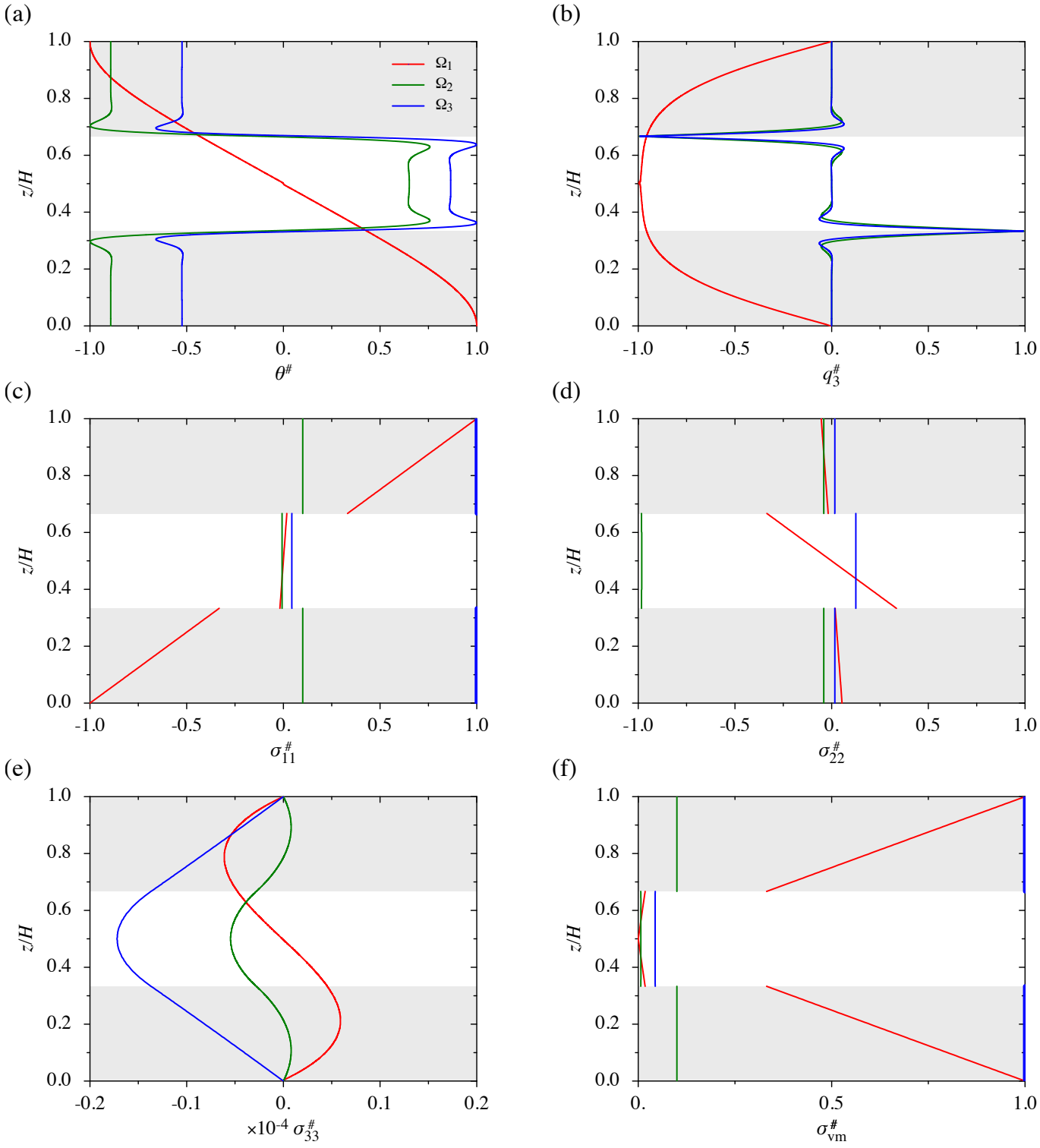

Figure 7: Through-thickness profiles of the first three mode shapes in the three-layered structure described in Fig. (6) at $x = L/2$.

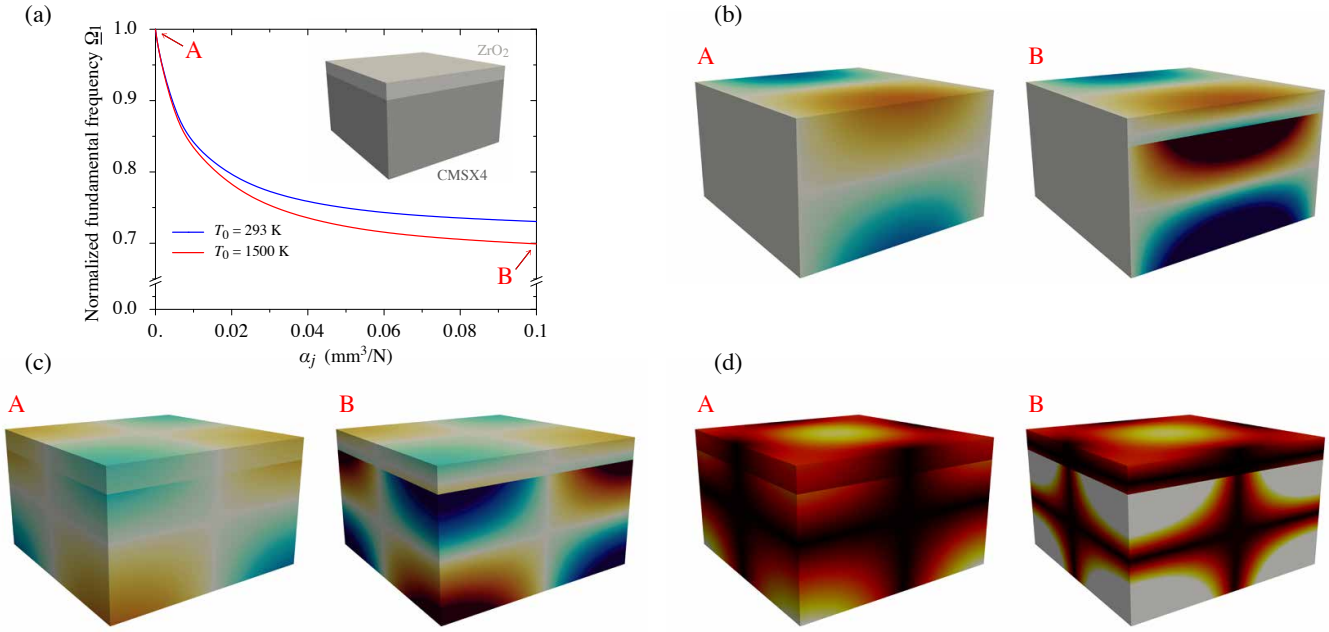

Figure 8: (a) Influence of the isotropic bonding stiffness coefficients α_j on the normalized fundamental frequency $\underline{\Omega}_1$ of the thermal barrier coated superalloy made of two layers (ceramic ZrO_2 and CMSX4) for two environmental temperatures $T_0 = 293$ K and 1500 K. Differences in the normalized (b) elastic displacement $u_1^{\#}$, (c) in-plane shear stress $\sigma_{12}^{\#}$, and (d) von Mises stress $\sigma_{\text{vm}}^{\#}$ for superalloys with perfect (left-hand side) and imperfect (right-hand side with $\alpha_j = 0.1$ mm^3/N) boundary conditions at the internal ZrO_2/CMSX4 interface. In (b) and (c) the minimum values ($= -1$) are colored in dark blue, while maximum values ($= 1$) are in red. In (d), minimum values ($= 0$) for the von Mises stress field are colored in white, while maximum values ($= 1$) are in red.

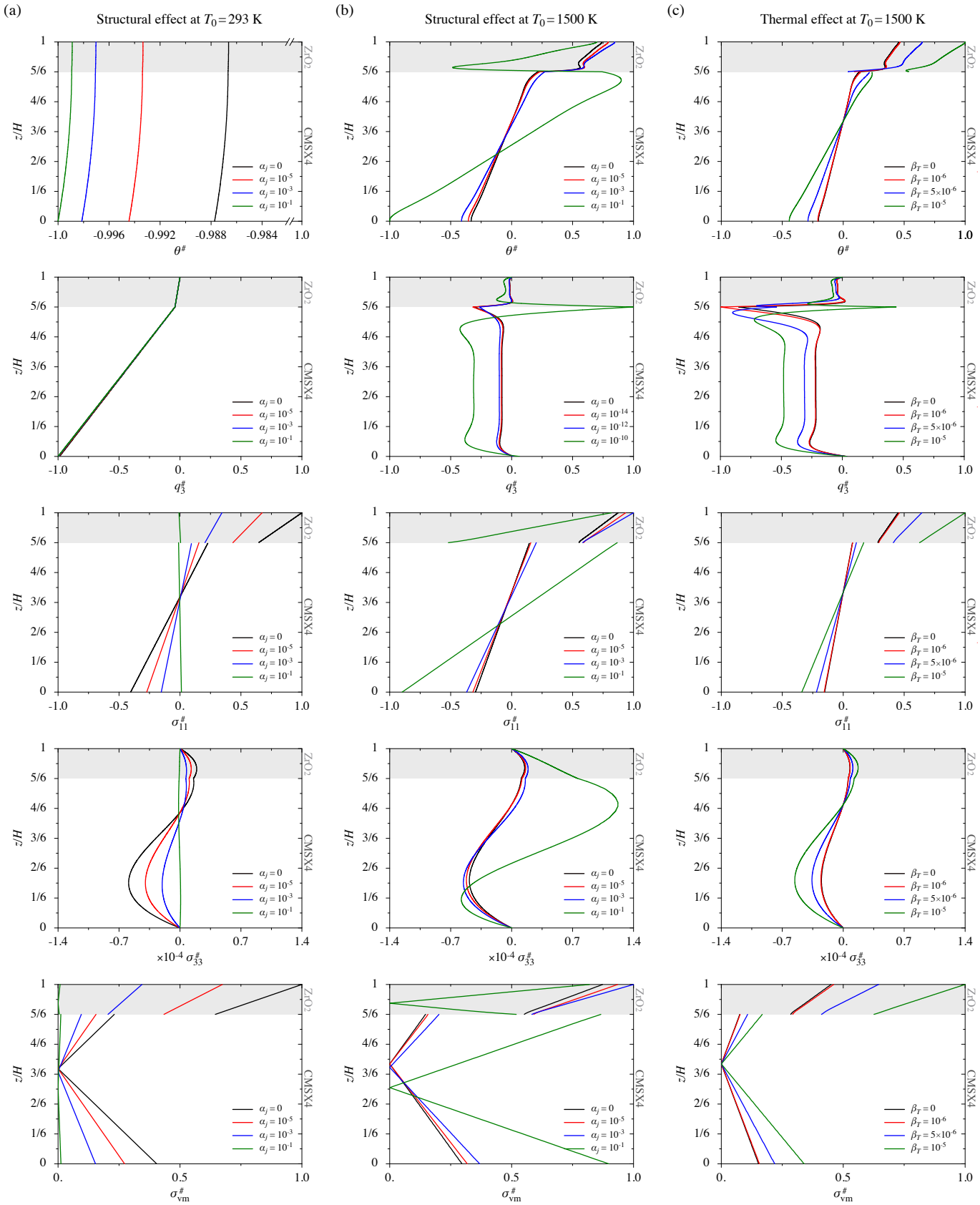

Figure 9: Effect of the imperfect boundary conditions in thermal barrier coated superalloys. Structural boundary conditions are applied at (a) $T_0 = 293$ K and (b) $T_0 = 1500$ K with different values of α_j in mm^3/N, while (c) thermal conditions are imposed at the weakly conducting ZrO_2/CMSX4 interface using the Kapitza model at $T_0 = 1500$ K with different value of β_T in Km^2/W. The black curves in all profiles are related to the perfect interfacial case.